


Summer 2017

BIOAVAILABLE IRON IN EQUATORIAL PACIFIC OCEAN AEROSOL SAMPLES

Hsiang T Teng
steng@yvcc.edu

Follow this and additional works at: <http://digitalcommons.cwu.edu/etd>

 Part of the [Analytical Chemistry Commons](#), and the [Environmental Chemistry Commons](#)

Recommended Citation

Teng, Hsiang T, "BIOAVAILABLE IRON IN EQUATORIAL PACIFIC OCEAN AEROSOL SAMPLES" (2017). *All Master's Theses*. 733.
<http://digitalcommons.cwu.edu/etd/733>

This Thesis is brought to you for free and open access by the Master's Theses at ScholarWorks@CWU. It has been accepted for inclusion in All Master's Theses by an authorized administrator of ScholarWorks@CWU. For more information, please contact pingfu@cwu.edu.

BIOAVAILABLE IRON IN EQUATORIAL PACIFIC OCEAN
AEROSOL SAMPLES

A Thesis
Presented to
The Graduate Faculty
Central Washington University

In Partial Fulfillment
of the Requirements for the Degree
Master of Science
Chemistry

by
Hsiang T. Teng
July 2017

CENTRAL WASHINGTON UNIVERSITY
Graduate Studies

We hereby approve the thesis of

Hsiang T. Teng

Candidate for the degree of Master of Science

APPROVED FOR THE GRADUATE FACULTY

Dr. Anne Johansen, Committee Chair

Dr. Dion Rivera

Dr. Yingbin Ge

ABSTRACT

BIOAVAILABLE IRON IN EQUATORIAL PACIFIC OCEAN

AEROSOL SAMPLES

by

Hsiang T. Teng

July 2017

Oceanic iron (Fe) fertilization experiments performed in remote regions have established that Fe additions draw carbon into the ocean, at least over the months-long time frame of the experiments. However, the mechanisms that control Fe speciation in atmospheric aerosol particles before and after deposition into the surface ocean remain largely unknown. This is in part due to the analytical challenge of quantifying Fe at environmentally significant sub-nano molar levels. The flow injection analysis method combined with the luminol chemiluminescence analytical system allows us to explore the near-real time determination of pico-molar levels of both Fe(II) and H₂O₂ produced from real marine aerosol particles collected over the Equatorial Pacific Ocean, as a function of both sunlight and electron donors (EDs) such as dimethyl sulfide and organic acids. Detection limits were as low as 40 pM Fe(II) and 100 pM H₂O₂. Fe(II) in aerosol concentration was found to be $0.29 \pm 1.48 \text{ pg m}^{-3}$ in large, $19.14 \pm 18.31 \text{ pg m}^{-3}$ in

coarse, $38.80 \pm 37.87 \text{ pg m}^{-3}$ in fine, and $43.61 \pm 42.93 \text{ pg m}^{-3}$ in ultrafine size aerosol samples. A typical analysis of photochemical reaction with addition of EDs can be performed in five minutes. Results indicate that Fe(III) is reduced in the presence of light with ED that are already present in the collected aerosols, the external additions of ED have an enhancing effect in some of the samples, and the Fe(II) concentration shows positive corrected to non-sea-salt sulfate (NSS-SO₄²⁻) and some other anions. Fe(II) is found to be 3% of total Fe in the aerosols. These results contribute to resolving current inconsistencies in chemical models on the speciation of Fe and sulfur cycles in the marine atmosphere.

ACKNOWLEDGMENTS

First and foremost, I am most thankful to my advisor, Dr. Anne Johansen, for supporting me in the development of my knowledge of chemistry, aiding in establishing my interest in the field of marine iron chemistry, and for always ensuring there was appropriate funding for my research. Throughout my Master's program, the patience she has had for me has allowed me to overcome, by far, the most challenging time in my life. I am most thankful for her excellent scientific insight, advice, and guidance, but I also deeply appreciate the kindness and humanity she has demonstrated as both a precise scientist and also an enthusiastic person. During the time I was completing my thesis, I was expecting my second son. She provided a flexible schedule allowing me the necessary time with my family. She has been an exceptional mentor to me for which I am grateful.

I am also thankful for the guidance and assistance of my dissertation committee members. I often came to Dr. Ge with mathematical questions and he has always been helpful by sharing his expertise. I am thankful for Dr. Rivera providing some important fundamental suggestions to promote, re-structure, and complete this thesis.

A special thanks to my friend, Robert Detloff who has helped me many times on proofreading this thesis. Without his assistance, this paper would never be documented.

I thank my family and especially my wife, Hoi Yi Ting. They had to work with my timeline, match my daily schedule, and help free me from other tasks to concentrate on finishing this thesis.

Lastly, I want to thank Central Washington University for making my work possible through the Master's degree program and the funding of the project provided through the NSF ECS-1149330 award.

TABLE OF CONTENTS

Chapter	Page
I INTRODUCTION.....	1
1.1 Carbon Cycle and Fe Fertilization of Ocean.....	1
1.2 Atmospheric Deposition of Fe	2
1.3 Aerosol Fe Solubility in Seawater	5
1.4 Fe Dissolution (Fed) Chemistry.....	8
1.5 Role of Organic ED and Hydrogen Peroxide	12
1.6 Flow Inject Analysis with Chemiluminescence	13
1.7 Goals of This Work	14
II EXPERIMENTAL METHODS.....	17
2.1 Experimental Design Overview	17
2.2 Samples and Sample Processing.....	19
2.3 Experimental Setup and Calibration.....	25
2.4 Solar Simulator	33
2.5 Fe(II) Concentration in Sampled Air Volume and 4 Size Fractions.....	34
2.6 Volume Weighted Averages	35
III RESULTS.....	36
3.1 Raw Fe(II) Data as a Function of Time	36
3.2 Fe(II) Concentration in Sampled Air Volume and 4 Size Fractions.....	39
3.3 Effect of ED Addition	46
3.4 Initial Fe(II) Concentrations in Relation to Naturally Present EDs	51
3.5 Percent (%) Fe(II)	54
IV DISCUSSION.....	56
4.1 Bioavailable Fe Concentrations in Aerosols and in Simulated Surface Water Over the Equatorial Pacific Ocean	56
4.2 Fe(II) Distribution as a Function of Aerosol Size and Region.....	58
4.3 Chemistry of Fe(II) Dissolution.....	61
4.4 Fe(II) Dissolution as Function of Naturally Present EDs	63
4.5 Percentage of Fe(II) to Total Fe	65

TABLE OF CONTENTS (CONTINUED)

Chapter	Page
V CONCLUSION.....	67
REFERENCE	69
APPENDIX.....	83

LIST OF TABLES

Table	Page
2.1 Timeline of steps in extraction experiment (0-285 seconds)	24
3.1 T-test of deviation from slope to slope using two-sample assume equal variance in 0.5 (pmol per second)	50
4.1 Comparison of Fe(II) and total Fe (Fe_{tot}) atmospheric aerosol concentrations in different regions.....	57
A1. Size resolved Fe(II) concentrations in five stages	83
A2. Size resolved atmospheric iron concentrations in the equatorial Pacific Ocean regions.....	85
A3. Volume weighted average Fe(II) concentration in various size fractions, stages and regions	86
A4. Summary of Fe(II) correlation to anions.....	87

LIST OF FIGURES

Figure	Page
1.1 Aerosol distribution is plotted using the particle numbers vs. the particle size.....	4
1.2 Deposition velocity vs. particle diameter	4
1.3 Iron pE/pH diagram showing the boundary in between each Fe species	6
1.4 Activities of single ion species and FeT activity (Darker line) in equilibrium with goethite as a function of pH	7
2.1 Based on the chemical characterization of the aerosols, the complete cruise track was divided into three different regions: North, Central, and West	21
2.2 High-volume collector with regulated pump.....	21
2.3 Four impaction and filtration substrates: large, coarse, fine, and ultrafine (white filter).....	22
2.4 Both samples and ED used in the experiments were kept in ice	25
2.5 The photochemical FIA-CL analytical experimental setup	26
2.6 Reaction vessel.....	27
2.7 FeLume (II) system	28
2.8 Flow Cell	29
2.9 PMT	29
2.10 Photon counts as a function of the standard Fe(II) from 10pM – 2000pM.	31

LIST OF FIGURES (CONTINUED)

Figure	Page
2.11 Photon counts as a function of the standard H ₂ O ₂ from 0.3 nM - 3.2 nM	33
2.12 Path length in units of Air Mass, changes with the zenith angle.....	34
2.13 Air volume (m ³) pumped through each sample	35
3.1 Raw real-time results of photon count for Fe(II) production	38
3.2 Stacked bar plots of Fe(II) concentrations for each size fraction	40
3.3 Five stages of Fe(II) changes from initial to ED2 nd	44
3.4 The volume weight average of Fe(II) in pg per m ⁻³ contributed from each fraction of filters	46
3.5 Photon counts vs. time for fine fraction of samples 28206 (top) and 28506 (bottom)	48
3.6 An example (Fine sample 23806) of slope determination at the various stages .	49
3.7 Regional and overall average of Fe(II) production rate changes with P value	50
3.8 Results from multivariate regression analysis are presented in bar graph	53
3.9 Regional and overall % Fe, all size fraction stacked bar graph. % .	55
4.1 Organic anions, oxalate and NSS-SO ₄ ²⁻ detected with the IC analyzing the same set of samples	59
4.2 Total Fe from each fraction using ICP-MS	66
A1. Rate of Fe(II) change for each sample sort by size fraction.....	88

LIST OF FIGURES (CONTINUED)

Figure	Page
A2. Fe(II) concentrations vs. various anions and total Fe (in ng m ⁻³).....	90
A3. Fe(II) contribution from first three stages in each sample	96
A4. Fe(II) contribution from last two stages in each sample	98

CHAPTER I

INTRODUCTION

1.1 Carbon Cycle and Fe Fertilization of Ocean

Phytoplankton are microscopic plant-like organisms that efficiently produce high biomass yields and promote organic matter fluxes into sedimentary deposits. In this process, phytoplankton absorb about half the global CO₂ via photosynthesis into the deep ocean, which becomes the world's largest carbon sink (Field, 1998). Although this oceanic biogeochemical cycle involving phytoplankton is hypothesized as playing a key role in the regulation of global temperatures (Behrenfeld, 2001), many scientific aspects of this process remain unanswered.

Many researchers have shown that iron (Fe) is an important co-factor that is essential for marine photosynthetic organisms, assisting in the cell's ability to grow, multiply (Geider and la Roche, 1994; Semeniuk et al., 2015), photosynthesize, and fix nitrogen (Morel, 2003). However, Fe(III), the most prevalent form, has very low solubility under oxidizing seawater conditions above a pH of 4 (Liu and Millero, 2002), but has been found to be able to accentuate the growth of phytoplankton in high-nutrient, low chlorophyll (HNLC) regions.

Three open ocean areas have been identified as HNLC regions, including the subarctic Pacific, the equatorial Pacific, and the Southern Ocean (Cullen, 1991; Coale et al., 1996; de Barr, 2005; Boyd et al., 2007). In these regions, primary productivity of

marine organisms is limited by Fe bioavailability (Martin and Fitzwater, 1988). Since 1993, twelve small scale Fe fertilization experiments, some conducted over months-long time frames (Behrenfeld et al., 1996; Boyd et al., 2007), were performed in HNLC regions and established data to prove that Fe additions indeed do promote phytoplankton blooming and withdraw atmospheric CO₂ into the ocean. Specifically, in one of the experiments performed in the sub-Antarctic Southern Ocean, the carbon flux within the Fe fertilized patch was found to be two to three times larger compared to the carbon fluxes from adjacent non-Fe fertilized HNLC areas (Pollard et al., 2009).

1.2 Atmospheric Deposition of Fe

It is not well understood how phytoplankton in remote regions receive their limited supply of the micronutrient Fe. Under natural circumstances, the open ocean receives little riverine inputs of Fe, more particularly in HNLC regions in which trace Fe is supplied either by upwelling of nutrient rich water or the deposition of Fe containing atmospheric particles (Martin and Fitzwater, 1988; Mahowald et al., 2007). Fe supply is hypothesized to be limited to the deposition of atmospherically derived Fe-bearing crustal aerosols originating from continental land masses (Ginoux et al., 2001; Mahowald, 2003; Tegen et al., 2004; Jickells, 2005b). Evidence also shows that eolian dust is the potential control factor of Fe fertilization in HNLC regions (Watson, 2001; Boyd and Doney, 2003). One has to consider that atmospheric transport of soil dust could be the main source of Fe to the remote ocean (Jickells et al., 2005).

Atmospheric dust contains significant concentrations of aerosol particles as high as 10^7 to 10^8 particles per cm^3 , and the diameters of these particles span from a few nanometers to 100 micrometers. That is, the mass of a 10 μm diameter particle is equivalent to the mass of one billion, 10 nm particles. The distribution of these particles in the atmosphere is determined by many factors, such as the removal process of the particles which are dry and wet deposition, condensation from, or evaporation to the vapor phase, and coagulation aerosol phase chemistry. Another important factor for the aerosol distribution is the distance from the source of the primary emission (Carslaw et al., 2013; Croft et al., 2014). The source of dust determines particle sizes. For example, automobile exhaust particles can be as small as a few nanometers, whereas wind-blown dust or sea salt are generally larger than one micrometer. While these atmospheric aerosols travel great distances, the dry or wet deposition of dust to the ocean is highly variable in both space and time (Jickells et al., 2005). Considering the marine aerosols distribution over HNLC regions, the size of these particles, as well as their physical and chemical properties, are important factors which affect their lifetime in the atmosphere (Baker and Jickells, 2006).

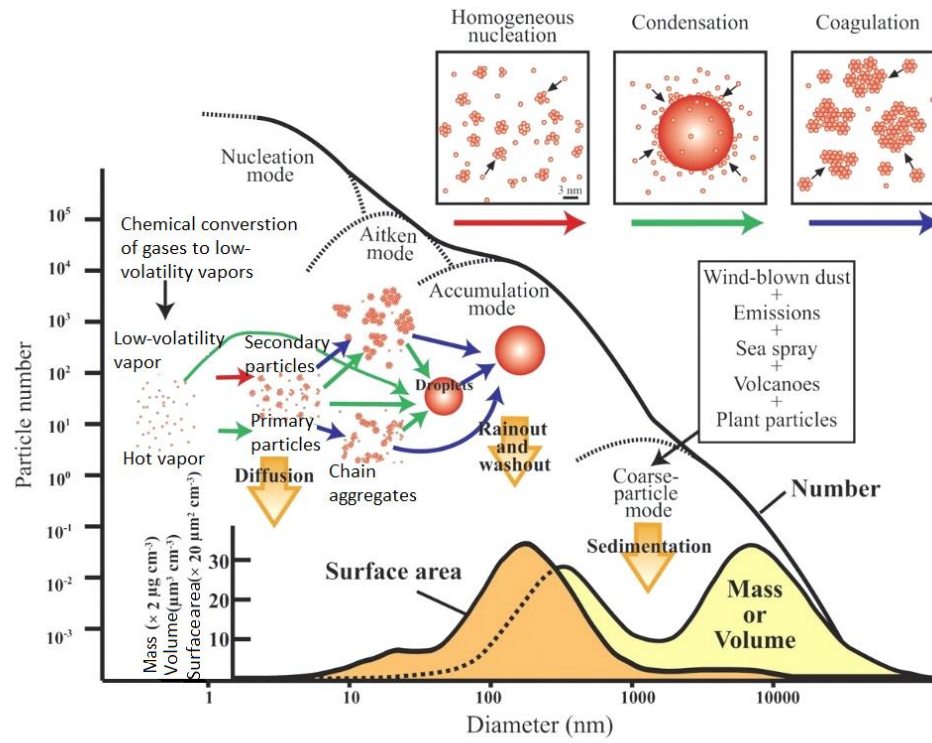


Figure 1.1 Aerosol distribution is plotted using the particle numbers vs. the particle size.

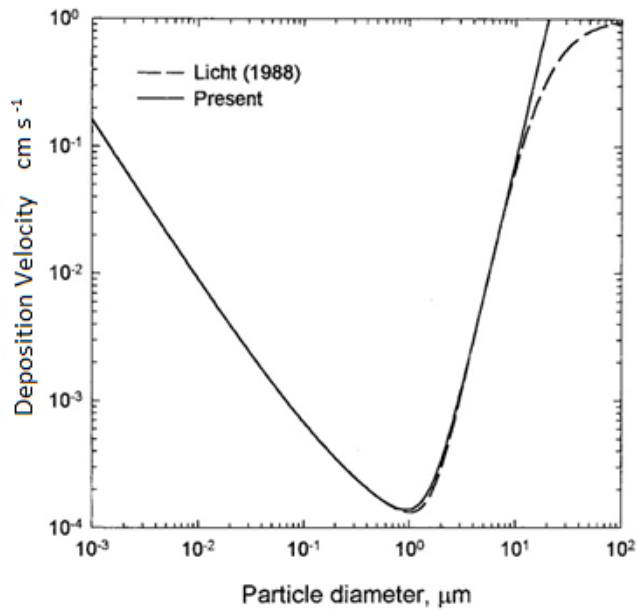


Figure 1.2 Deposition velocity versus particle diameter

1.3 Aerosol Fe Solubility in Seawater

Fe in mineral dust must dissolve into the ocean to become bioavailable Fe; however, the process of dissolution remains a key uncertainty in our understanding of the marine Fe cycle. In a dissolved Fe simulation study, mineral dust deposition was found to provide ~0.26 Tera grams (Tg) ($1 \text{ Tg} = 10^{12} \text{ g}$) of dissolved Fe into global oceanic regions per year (Johnson and Meskhidze, 2013) and it has been estimated that bioavailable Fe is 1-5% of total Fe that is present in the marine environment (Sunda, 2001; Johansen and Hoffmann, 2003; Shaked, Kustka, and Morel, 2005).

Numerous studies have been performed to increase our understanding of the factors that influence Fe solubility in both the atmosphere and ocean. Many of the factors include, aerosol source (Journet et al., 2008; Sholkovitz et al., 2012), aerosol size (Johansen, Siefert, and Hoffmann, 2000; Buck, Landing, and Resing, 2010), oceanic pH/ atmospheric processing (Solmon et al., 2009; Shi et al., 2012), photochemical processing (Johansen and Key, 2006; Fu et al., 2010), Fe binding ligand compounds (Buck, Selph, and Barbeau, 2010; Boyd, Mackie, and Hunter, 2010; Hassler et al., 2010), and biological processing (Boyd et al., 2010; Konhauser, Kappler, and Roden, 2011).

In the atmosphere, most Fe mass is associated with Fe oxides and hydroxides contained in mineral dust aerosols that are emitted from continental sources. Fe oxide in atmospheric mineral dust particles is primarily composed of Fe together with O and/or OH in the form of oxyhydroxides and hydroxides, such as goethite ($\alpha\text{-FeOOH}$), and oxides, such as hematite ($\alpha\text{-Fe}_2\text{O}_3$) and ferric Fe (Fe(III)) as part of aluminosilicates (Barrón and Torrent, 1996). Fe speciation ranges from most soluble Fe(II) (Shaked et al,

2005) to the most insoluble Fe(III) species (Baker and Croot, 2010). Fe in mineral dust tends to be in the form of the thermodynamically stable Fe(III); it also tends to hydrolyze or combine to form (1) inorganic Fe oxide species: Fe(III) (hydr)oxide and oxyhydroxide complex or (2) organic ligand complexes. The precipitation of Fe(III) (hydr)oxide species depends on pH (Kenshi Kuma, Jun Nishioka, and Katsuhiko Matsunaga, 1996) and the reduction potential (pE) of the solution (Fig 1.3).

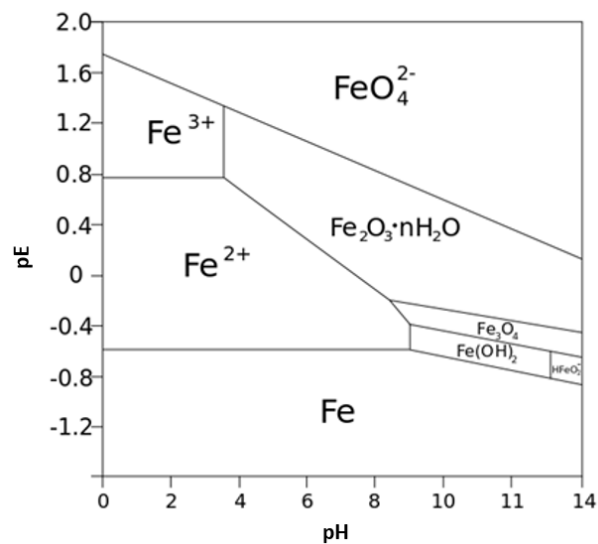


Figure 1.3 Iron pE/pH diagram showing the boundary in between each Fe species.

As mentioned earlier, not all forms of Fe are bioavailable in the surface waters of the ocean and only the soluble forms of Fe are bioavailable (Martin et al., 1994; Coale et al., 1996; Sunda, W.G. 2001). Fe speciation defines its biogeochemical characteristics thereby determining its role in oceanic Fe cycle and bioavailability (Trapp, Millero, and Prospero, 2010). This means that only at the extreme pH values, these compounds maintain a very low level of total Fe (Fe_T) in solution. The solubility of Fe as the function of pH can be illustrated by plotting the logarithmic activity of the components of Fe_T as a

function of pH (Fig 1.4), goethite as an example. Above pH 4, most hydrolysis species become increasingly stable and move towards higher concentrations than the solubility product, i.e. of $\text{Fe}(\text{OH})_3$, alone.

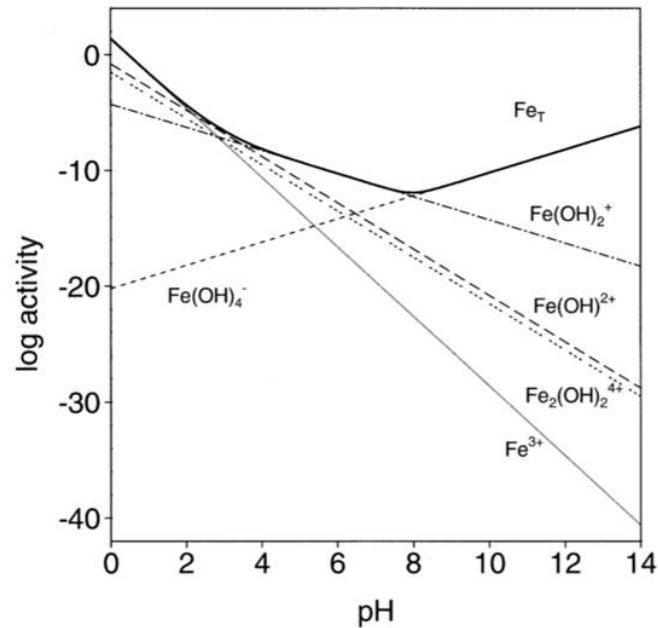


Figure 1.4 Activities of single ion species and Fe_T activity (Darker line) in equilibrium with goethite as a function of pH (Cornell, Rochelle and Schwertmann, 2003).

$\text{Fe}(\text{III})$ oxyhydroxide species have very low solubility in seawater forming a colloidal Fe pool on the ocean surface (Liu and Millero, 2002). In this regard, the general and operational definition of each category of soluble Fe is based on their particle size, in which dissolved Fe (Fe_d) ($\text{Fe}_d < 0.2 \mu\text{m}$) plays an important role as bioavailable Fe. Fe_d includes two sub-categories: small particulate colloidal Fe (Fe_c) ($10 \text{ kDa} < \text{Fe}_c < 0.2 \mu\text{m}$) and truly dissolved soluble Fe (Fe_s) ($\text{Fe}_s < 10 \text{ kDa}$) size fractions (Fitzsimmons et al., 2015). Although Fe_c contributes to most total Fe_d across the global ocean, very limited Fe_c forms are found to be bioavailable Fe (Hassler et al., 2011). For example, crystalline

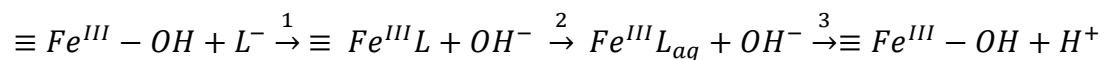
inorganic Fe_c is not available to marine phytoplankton directly (Rich and Morel, 1989). On the other hand, most forms of Fe_s are readily accessible to marine organisms (Chen et al., 2003; Wang and Dei, 2003), these include Fe(II) and Fe(III) organic ligand complexes. Complexation of Fe(III) with ligands (Fe_L) also plays a significant role in the open ocean Fe cycle. The existence of strong and weak Fe_L pools has been determined by using electrochemical methods (Rue and Bruland, 1995), where siderophore-like molecules seemed to be the most stable binding ligands (Gledhill et al., 2004). However, their concentrations are typically very low relative to the total Fe_L concentration pool (Mawji et al., 2008). It was found that low-molecular-weight (LMW) organic ligands are more abundant (Gerringa et al., 2006) because of the accumulation of organic matter such as extracellular polymeric substances (Hassler et al., 2011) and cellular debris (Hutchins et al., 1999) from marine microorganisms. Significant evidence exists that supports the understanding that Fe_L increases Fe solubility on the ocean surface waters. (Gledhill and Buck, 2012; Lannuzel et al., 2015).

1.4 Fe Dissolution (Fe_d) Chemistry

Three main physical and chemical mechanisms that promote dissolution Fe have been reviewed (M.S. Johnson and N. Meskhidze, 2013): (i) proton promoted Fe(III) dissolution, ligand-promoted Fe(III) dissolution, and reductive of Fe(III) dissolution. Proton-promoted mechanism is the result of the breakage of Fe-oxygen (Fe-O) bonds by protonation of oxygen atoms and/or hydroxyl groups at the mineral surface which form $[(Fe(OH)_{(3-n)})^{n+}]$ (Stumm and Furrer, 1987). Fe-O bonds are normally seen in crystal lattice structures as FeOOH. This reaction happens specifically at the surface of the OH group.

The Fe-O bond is weakened by the proton adsorption on the OH groups, leading to the detachment of Fe atoms from the surface of the crystal lattice. It is a very slow process relying on low pH (< 1) and, on the contrary, the stable form of Fe crystal lattice is regenerated when pH is raised (> 2) (Samson and Eggleston, 1998). Since oceanic pH values are generally high (> 8) due to the large buffering capacity of CaCO₃, proton-promoted dissolution could be considered as a minor process of Fe(II) contribution.

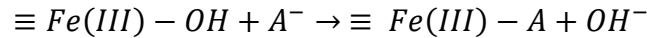
Ligand-promoted Fe dissolution may follow an analogous mechanism by weakening the Fe-O bond. Some anions (e.g. Cl⁻, SO₄²⁻) or organic compounds (e.g. oxalate) have better affinity than protons and can form ligands at the surface of Fe oxides to replace the OH groups (Cornell et al., 1976). Unlike proton adsorption, ligand adsorption to form complexes of organic and inorganic ligands at the surface of Fe oxides is generally weaker than covalent bonds. These ligand complexes may accelerate, decrease, or terminate the ligand-promoted dissolution process depending the level of pH. The dissolution process may be promoted by adsorption or complexation with Fe (Fe^{III} L_{aq}) in the solution (Salfity et al. 2000). The overall reaction is as below.



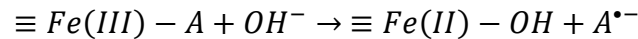
Where $\equiv Fe^{III}$ is the hydrolyzed Fe at the outside surface of the Fe particle, L⁻ is the deprotonated ligand. Step 2 leaves a fresh $\equiv Fe^{III}$ exposed and to be hydrolyzed by H₂O forming $\equiv Fe^{III} - OH$. The rate of ligand-promoted dissolution varies with the pH of the solution and type of ligands present, i.e. number of bonds. In general, optimal acidity for ligand-promoted dissolution is higher than proton promoted dissolution. For example,

the rate of Fe dissolution from hematite in oxalic and citric acid was maximized at pH 4-5 (Zhang et al., 1985). As seen in Step 3, when pH falls, there is a reversed Fe dissolution and Fe oxide reforms (Stumm and Furrer, 1987).

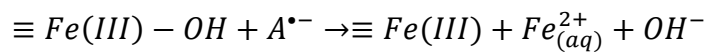
Reductive dissolution involves reductants and electron transfer which may be the most complex and important Fe dissolution mechanism in marine environments. The kinetic study of reductants reacting with Fe oxide species aids to understand the complexities of the reductive dissolution process. The classical concept of reductive dissolution of Fe oxide has been assumed to start at reversing surface complexation in which a dissolved reductant (A^-) is adsorbed to the oxide's surface (Faovre, 2016). The tendency of reductants to deprotonate in natural systems has been investigated and reviewed, such as ascorbic acid, cysteine, hydroquinone, H_2S , methanesulfinic acid (MSA), oxalic acid, etc. (Cornell, Rochelle and Schwertmann, 2003).



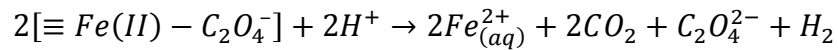
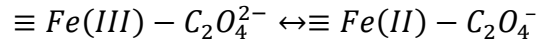
This reaction is followed by an electron transfer from the ligand to Fe(III), ligand-to-metal charge transfer (LMCT) (Miller et al, 1995) and an oxidized radical is produced.



The radical reacts with another OH group at the surface of Fe-O and the Fe(II) is detached.

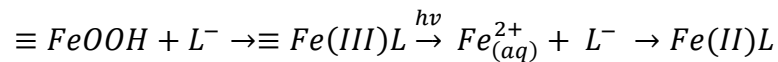


Organic ligands also play a role as ED to the reductive dissolution. For example, oxalate organic complexation in the addition of Fe(II) to the system would promote electron transfer via a surface complex and accelerate dissolution (Paris, Desboeufs and Journet, 2011).



1.4.1 Photochemical Reduction

Photochemical electron transfer on surface Fe(III)-organic ligand complexes provide an additional pathway for dissolution. Much evidence shows that the presence of organic Fe-complexing ligands and UV/visible radiation promote higher fractions of Fe_d in seawater (Cornell, Rochelle and Schwertmann, 2003).

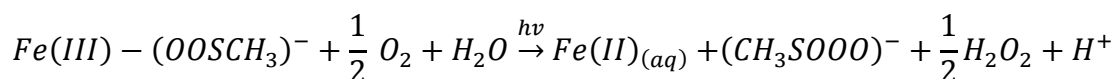


In natural waters it is well known that the carboxylate group [RC(O)O⁻] is one of the most common functional groups found in the dissolved organic compounds (Thurman, 1985; Perdue and Gjessing, 1990) such as the dicarboxylic acids (e.g., oxalate, malonate, and citrate) forming strong complexes with Fe³⁺ which absorbs a wide range of wavelengths that proceeds the photochemical reactions in sunlight (Duckworth and Martin, 2001). Other organic ligands such as formate, acetate, and methanesulphinic acid (MSIA) play an important role in promoting the photo-reductive dissolution of Fe (Johansen and Key, 2006).

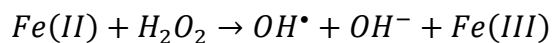
Organic ligands involve both “ligand-promoted Fe dissolution” and “reductive dissolution” processes to distinguish them in the context of the reduction of structural Fe_L in a surface Fe_L complex followed by Fe(II) detachment and the formation of a soluble Fe (III) ligand (aq) complex followed by its reduction in solution. It may be that the two processes are kinetically equivalent (Borghi et al, 1991).

1.5 Role of Organic Electron Donor (ED) and Hydrogen Peroxide

Under natural circumstances, Fe(II) released from an aerosol particle into seawater, upon deposition, would be rapidly hydrolyzed and precipitated into an Fe(III) oxidation state with the reaction having been promoted by photochemically generated H₂O₂. In a kinetics study the reduction of Fe(III) by peroxide was not observed in the pH range 7-8 (Moffett and Zika, 1987). In general, Fe(II) has higher solubility than Fe(III) in seawater. This low concentration of Fe(III) could be the reason for the presence of different levels of hydrogen peroxide and organic compounds that act as the main factors of Fe_d levels in atmospheric aerosols and cloud droplets in the case of light-induced photochemical redox of Fe (Chen and Siefert, 2003; Fu et al., 2010). For instance, this photochemical reductive dissolution is associated with MSA and the production of H₂O₂. The chemical equation is as follows. (Johansen and Key, 2006)



Fe(II) can be consumed during the subsequent production of H₂O₂, and the H₂O₂ produced is capable of further oxidation of Fe(II) in what is known as the Fenton reaction (Zepp et al., 1992; Arakaki and Faust, 1988; White, Vaughan and Zepp, 2003).



Since the production of H_2O_2 will oxidize $Fe(II)$, Fe_d concentration levels are hypothesized to be stabilized by other organic components. In the current study's model, organic aerosol components seem to play an important role on aerosol Fe solubility (Smoydzin and von Glasow, 2007; Aumann and Tabazadeh, 2008). However, more measurements of organic surfactants, in particular their concentrations, is required to draw any specific conclusions. Above the surface of seawater, a feedback mechanism is hypothesized between phytoplankton induced organic substance emissions and Fe starvation. Organic substances such as DMS and isoprene, or its oxidation products - MSIA and oxalic acid, may play a significant role in generating bioavailable $Fe(II)$ and oxidative H_2O_2 (Johansen and Key, 2006).

1.6 Flow Inject Analysis with Chemiluminescence

The measurement of unfavored, thermodynamically unstable $Fe(II)$ in seawater has become important evidence in showing the Fe dissolution process in seawater, however difficult to achieve. The detection limit (DL) of $Fe(II)$ present as the primary challenge of photochemistry of organic $Fe(III)$ complexing ligands study since Fe chemistry is largely controlled by the extremely low solubility of all $Fe(III)$ oxy(hydr)oxides. To better understand the Fe redox cycle over seawater, it is necessary to measure $Fe(II)$, which is limited to pico- to sub-nanomolar concentrations in surface ocean. However, most studies have been limited to measuring Fe concentrations in micromolar (μM) or nanomolar (nM). Here, experiments were

performed using flow-injection analysis with a chemiluminescence detection (FIA-CL) method. An FIA-CL instrument has been developed (FeLume – Waterville Analytical, Waterville, ME) to determine sub-nanomolar concentrations of Fe(II) in the different types of natural waters (Emmenegger et al., 1998). One of the advantages of using FIA measurements is being able to develop a simultaneous measurement with optimized methods of chemical reaction, carried out under flow conditions (Trojanowicz and Kołacińska, 2016). When the Fe is free from organic matter in the sample, the relationship between chemiluminescence and Fe(II) is approximately linear. However, it has been suggested that the chemiluminescence of Fe(II) results from CL analysis of freshwater samples will be impacted by the interferences of reagent with dissolved organic carbon (DOC) in the solution (Pullin and Cabaniss, 2001; Rose and Waite, 2001).

1.7 Goals of This Work

Current studies focus on understanding the formation of Fe_d from mineral dust during the transport from land to ocean in the air. Multiple factors account for the changing rates of dissolution of Fe oxides in the marine system: the system itself (temperature, UV light), the composition of the solution (pH, redox potential, acid, reductant and complexing agents), and the properties of the oxide (surface area, stoichiometry, crystal chemistry). Most Fe dissolution kinetics data has been obtained from laboratory studies; however, an experimental model that can reestablish a comprehensive natural system and mimic the chemical mechanisms of the open ocean is not yet available. More specifically, the recent studies on the photochemical Fe redox

cycle in seawater has been reviewed by Barbeau K. (Barbeau, 2006). Improvements and challenges of this type of study were pointed out. Most of work was done in Fe- and dissolved organic matter (DOM)-enriched coastal or estuarine environments or in Fe fertilized water. The high concentration of organic compounds preexisting in the analyte must be considered. These chemicals are counted as factors in the Fe redox chemical cycle which should be excluded as much as possible to better understand the role of organic compounds in the Fe dissolution process, for two reasons. DOM could affect the sensitivity of the analytic results, and preexisting DOM is promoting Fe(III) dissolution thus initial Fe(II) concentration is difficult to obtain. Other than the consideration of the analyte, much of evidence shows the potential importance of colloidal size class as an important contributor of Fe(III)-binding ligands in some marine environments (Wu, 2001). To investigate this, a stimulated study using a low Fe concentration sample, such as open ocean as background, will be necessitated.

To summarize, much work of this research aimed to fulfill the short pieces of evidence in the study of photochemical Fe redox cycle in seawater. That is, to determine the reductive photochemical dissolution of Fe in real marine atmospheric particles. The availability of highly sensitive FIA-CL techniques for measurement of analytes brings increased potential for studies of Fe photo-reduction in systems reflective to neutral pH conditions. Although to achieve Fe dissolution by kinetic study in the laboratory, it is important to mirror the natural pH of seawater to reach a reasonable reaction rate due to the consideration that the majority of electrons are contributed from the metabolic oxidation of organic compounds of ecosystems near the ocean's surface with a reliable

average pH of 8.2. However, the matrix effect of seawater would also influence the sensitivity of the CL luminol method. Pure water of near neutral pH was necessary to use in this study. A photochemical Fe dissolution reaction was mimicked in the clean laboratory: analyte samples were collected from HNLC regions where the matrix effect was minimized and the products Fe(II) and H₂O₂ were measured via an FIA-CL method to quantify both chemicals at sub-nanomolar concentrations in pure water to avoid the DOM effect. Results from this model helped us better understand the chemistry of aerosol Fe solubility and also to describe the complex systems involved in many of these factors.

CHAPTER II

EXPERIMENTAL METHODS

2.1 Experimental Design Overview

The objective of this research is to determine the reductive photochemical dissolution of iron in real marine atmospheric particles under environmental conditions mimicking surface ocean water. In addition, the relative importance of various ED is investigated, as well as the production of H_2O_2 . The most challenging aspect of this work is the analytical component, as environmental concentrations of Fe(II) and H_2O_2 are at sub-nanomolar and nanomolar levels, respectively, which require state-of-the-art instrumentation and clean environments. To accomplish this, a low concentration seawater condition had to be mimicked. The flow injection analysis system with chemiluminescence detection (FIA- CL) provided the necessary analytical sensitivity, while working in the clean lab in a laminar flow hood assured a low background working environment. Our methods are based on those developed and optimized by D.W King et al., (1995) and are based on the chemiluminescence of Luminol with Fe(II) and Acridinium Ester (AE) with H_2O_2 (D. W King et al., 2007). This analytical system provides an essential advantage to the study of oceanic low concentration seawater samples by being faster and far more accurate than other methods. This improved speed and accuracy aided in determining the effects of various ED in dark and irradiated seawater samples on the production of Fe(II) and H_2O_2 concentrations in sub-nanomolar concentrations every 0.33 seconds during dissolution experiments. It is imperative that

these experiments were carried out at such low and representative concentrations as otherwise Fe(III) would be largely controlled by its low solubility.

First, we investigated the DL of the chemiluminescence reactions of both the Fe(II)/ luminol and H₂O₂ /AE systems using the FIA-CL setup, and consistent results were obtained. Real aerosol samples with synthetic seawater were tested. Results from these experiments aided us in designing further experiments with real field marine aerosols in real seawater that had been stored at 4°C from past cruises.

In our setup, it was found that the matrix effect from both artificial and real seawater significantly reduced detection signals, which made analysis of real samples very difficult. In the end, to obtain detectable and reproducible signals, we analyzed all aerosol samples in pure water. Throughout the dissolution experiments of the aerosol sample, Fe(II) and H₂O₂ were analyzed in dark and light as well as after addition of various potential ED including dimethyl sulfide (DMS), isoprene, methanesulfinic acid (MSIA), and oxalic acid.

The general experimental setup consisted of extracting a previously collected marine aerosol sample into pure water to mimic the deposition of aerosol onto seawater at environmentally realistic concentrations. A 50.0 mL Teflon container was used as the reactor vessel. Sample aliquots were removed semi-continuously throughout the 285 second experiment and pumped directly into the dual channel (FIA Fe(II) and H₂O₂ analysis - see section 2.3.2 and section 2.3.3). The sample was allowed to

react in the dark, under simulated sunlight, and with ED. Following are detailed descriptions of the source of the samples, the analytical methods, and data analysis.

2.2 Samples and Sample Processing

2.2.1 Aerosol Samples

Field sampling was carried out by Lindsey Shank, a former MS. Student, and took place over the tropical north and equatorial Pacific Ocean between Honolulu, Hawaii, and Rabaul, Papua New Guinea. The cruise track is traced in yellow color (Fig 2.1). The two-month long cruise started in Honolulu, Aug. 17, 2006, and continued west along the Equator toward the Bismarck Sea, where it looped around and stopped in Rabaul on Oct. 1, 2006, for a few days and then transected back to Honolulu, on Oct. 17, 2006.

A high-volume collector (ChemVol 2400, Thermo Fisher Scientific Inc., Waltham, MA) (Fig 2.2) was operated at an average flow rate of 9.6 mL min^{-1} , fractionating aerosols into four size fractions. For the purpose of the present study, the following definitions for the individual size fractions were employed: large particles with aerodynamic diameter (d_a) $\geq 10 \text{ }\mu\text{m}$; coarse, $1 \text{ }\mu\text{m} \leq d_a < 10 \text{ }\mu\text{m}$; fine, $0.1 \text{ }\mu\text{m} \leq d_a < 1 \text{ }\mu\text{m}$, and ultrafine particles (UFP), $d_a < 0.1 \text{ }\mu\text{m}$ (Fig 2.3). The large, coarse, and fine size fractions were collected by impaction onto polyurethane foam (PUF) substrates, and the ultrafine size fraction were collected in the final filtration step onto polypropylene filters. The collector was set up on the top deck above the bridge and the vacuum pump was controlled via a relay box and data logger (CR1000, Campbell Scientific Inc., Logan, UT) so that the pump would stop when either (i) the wind speed dropped below 0.5

ms⁻¹, (ii) the wind direction was unfavorable (i.e., 60° off either side of the bow, to prevent contamination from the ship's engine plume), or (iii) during precipitation episodes. The 38 sets of samples were collected over the entire two-month cruise. Each sample set consisted of one large, one coarse, one fine, and one ultrafine substrate. In addition, five field blanks of each substrate were used for blank subtractions. These field blanks had been processed in the same way as the samples but without collection. Samples were labeled with the date and year of the initial sampling day (DDYY) in coordinated universal time. The 38 collected sample sets were divided into three regions: including samples 23206-23506, 28306-28806 at North region (11), 23606-26706 at Central region (13) and 26806-28106_2 at West region (11) (Fig 2.1).

All tools and equipment used in the sampling and analysis process were acid cleaned. Substrate changing and handling took place in a portable, clean, laminar flow hood with HEPA (High Efficiency Particulate Air) filtration (Air Control Inc., Henderson, NC). Trace-metal clean techniques were employed at all times. After collection and until analyses in the CWU clean laboratory, samples were stored at -20 °C in Petri dishes sealed with Teflon tape and double-bagged in two acid-cleaned plastic bags.

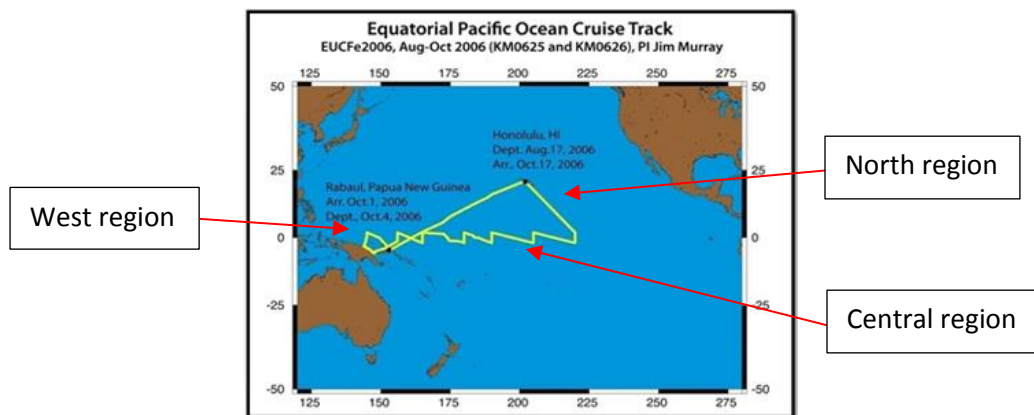


Figure 2.1 Based on the chemical characterization of the aerosols, the complete cruise track was divided into three different regions: North, Central and West.



Figure 2.2 High-volume collector with regulated pump.



Figure 2.3 Four impactation and filtration substrates: large, coarse, fine and ultrafine (white filter).

For each of the 38 sample sets, every size fraction was analyzed independently and in the following sequence: fine, coarse, large and ultrafine fractions. Samples were retrieved under a dust free environment. Tools for processing samples were acid washed and stored inside the fume hood prior to use. For analyzing samples and avoiding contamination, the outer bag of the double-bagged petri dishes was removed outside the clean hood. Thereafter, petri dishes were set into the laminar flow fume hood with the second layer of bagging that had not touched any surface outside the hood. Then, petri dishes were moved from the bag and set indirectly on an ice bath with a layer of acid washed plastic bag in between the dishes and ice (Fig 2.4). To avoid exposure of samples to air for prolonged times, the Teflon tape was removed from the petri dishes immediately before the analysis and a 1/6 of the fraction of the sample substrate was cut with ceramic scissors for analysis. The sample piece was transferred into a syringe (Norm-Ject, 10 mL) with Teflon forceps.

2.2.3 Sample Extraction

To prevent the potential bias in the experimental outcome due to the differing size and material of sample substrates, the samples were extracted before analysis and the substrate discarded. This was accomplished by adding 10 mL of extracting solution to the syringe containing the sample substrate fraction and pushing it into the reactor vessel thereby squeezing the sample substrate. This process was repeated four more times to make a total 50.0 mL of aerosol sample solution [1] (Fig 2.5). As mentioned above three types of extracted solutions were tested: real seawater, synthesized seawater and pure water. Immediately after squeezing the 5th 10 ml of solution through and out of the sample, which took about one minute, collection of data commenced. Each sample was analyzed in 4 stages. As shown in Table 2.1, stage 1 consisted of the dark reaction between time 0-20 seconds, stage 2 consisted of the light reaction, for which the solar simulator was turned on at time 21 seconds (it remained on until the end of the experiment), at stage 3 the pump was stopped for about 10 seconds for the addition of the DMS and isoprene mixture, and at stage 4 the pump was stopped again for the addition of the MSIA and oxalic acid ED mixture. During the 285 second, of one entire experiment, 855 data points were collected for Fe(II) and H₂O₂ each. Due to the fact that the FIA continues collecting data in between each step, even when the pump was stopped, approximately 30 seconds of data were removed when the pump was stopped for ED addition. Control experiments and field blanks were running samples to establish a true background signal.

Table 2.1 Timeline of steps in extraction experiment (0-285 seconds)

Stages						
	1	2	N/A	3	N/A	4
	Dark	Light	(pump stopped)	1st addition data	(pump stopped)	2nd addition data
Time (seconds)	0-20	20-75	Data 75-105 85: 1 st ED addition	105-180	Data 180-210 190: 2 nd ED addition	210-285

2.2.4 Electron Donors

As described above, after 75 seconds of leaching and analysis (more details on this in section 2.3), several potential ED were manually added in sequence into the aerosol sample solution. The chosen ED were biologically derived molecules DMS and isoprene as well as two of their oxidation products that have shown to photochemically reduce Fe(III) to the more soluble Fe(II) namely MSIA and oxalic acid (Johansen and Key, 2006). To accomplish this, concentrated ED solutions were prepared and kept stored in the refrigerator ($\leq 4\text{C}^\circ$) for up to four weeks. During the experiments, bottles of these solutions were kept capped on an ice bath in the fume hood until the addition into the sample. Acid washed pipette tips were used to transfer solutions. Twice (Table 3.4), the pump was stopped and concentrated solution was added to the reactor vessel; first DMS and isoprene were added, then MSIA and oxalic acid were added. Due to the limited amount of sample material, ED was added in sequence to the same sample instead of running a separate experiment. The effective concentration of the ED was calculated based on the volume of the remaining sample solution, which was approximately 38 ml at time 75 seconds, and 21 ml at time 180 seconds. The ED

concentration was chosen based on average concentrations of these chemicals found in the surface ocean: 5.0 nM DMS (Watanabe, Yamamoto and Tsunogai, 1995) (Alfa Aesar, 99+ %); 150.0 pM isoprene (Yoko Yokouchi et al., 1999) (Alfa Aesar, 99%); 5.0 nM MSIA (Alfa Aesar, 95%); 34.5 nM oxalic acid (Fluka, ACS; $\geq 99.5\%$). The four-concentrated stock solutions were prepared in different concentrations to make the desired concentration while adding into the solutions. In the sample, 70 μL of DMS (2.70 mM) and 10 μL of Isoprene (0.57 nM) was added first and 75 μL of MSIA (1.40 mM) and oxalic acid (9.66 mM) were added second.



Figure 2.4 Both samples and ED used in the experiments were kept on ice.

2.3 Experimental Setup and Calibration

2.3.1 Apparatus

The photochemical FIA-CL analytical experimental setup is shown in Fig 2.5. During the 285 seconds experiment, data points were set to collect every 0.33 second by the RS-232 interface (Waterville Analytical) for both Fe(II) and H_2O_2 on Window XP.

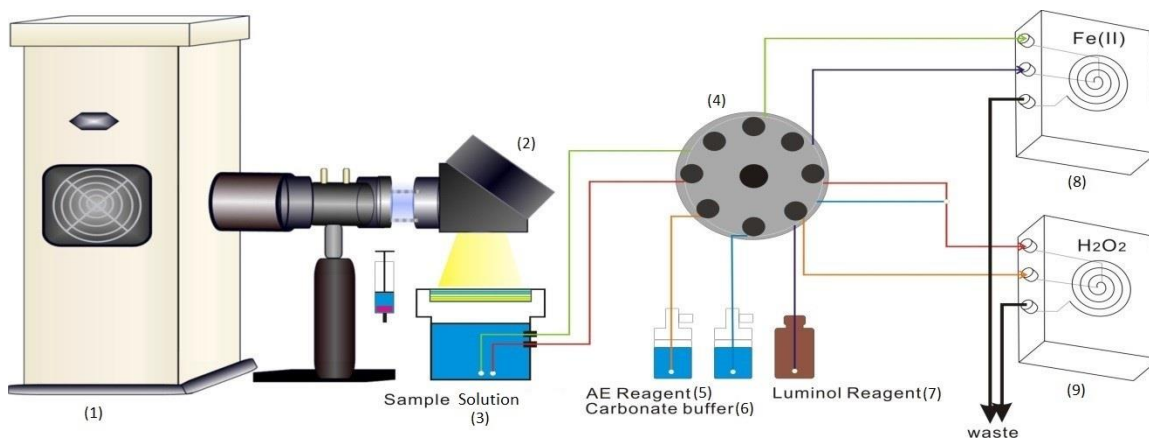


Figure 2.5 The photochemical FIA-CL analytical experimental setup.

Two small holes in the Teflon reactor vessel (Fig 2.6) (3) provide access for continuous withdrawal of extractant solution that is pumped with a peristaltic pump into the analytical system. The photo-simulator (1) provided the power density of 1353 W m^{-2} of energy representative of sunlight at the equatorial region, to the reaction vessel with a 90° mirror (2). The dual-reagent and continuous flow injection hardware setup is described as follows: A sample or standard was placed in the reaction vessel (3); the pump (4) (Dynamax) distributed both reagents and samples at a flow rate of 9.6 mL min^{-1} with a 0.3 mm id Teflon tubing (Idex) to the reactor cells (8,9); luminol reagent (7) was loaded through a reagent flow stream to mix with a sample solution in the Fe(II) reactor cell (8); the carbonate buffer (6) was combined with the H_2O_2 sample flow stream and mixed with the AE reagent (5) flow stream in the H_2O_2 reactor cell (9). Photons emitted in the flow cells were counted by two photon multiplier tubes (PMT) (Fig 2.9) and the signal was sent to the computer for recording and processing.

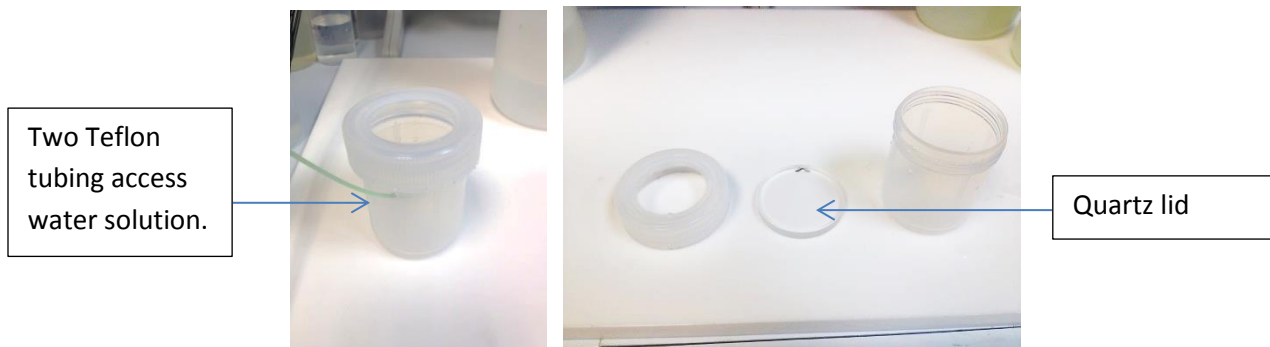


Figure 2.6 Reaction vessel

A 50.0 mL Teflon flask container was fitted with a quartz lid as the cover to allow the solar simulated light to penetrate into the water sample solution. A few centimeters from the bottom of the flask, two small holes provided access for two identical Teflon tubes of 0.3 mm diameter through which sample solution was pulled with a peristaltic pump for Fe(II) and H₂O₂ analysis.

2.3.2 FIA-CL System for Fe(II) Analysis

The FeLume (II) (Waterville Analytical) (Fig 2.7) was used as an automated flow injection analysis (FIA) system for the determination of Fe(II) by detection with luminol chemiluminescence reaction. Instead of directly determining the Fe(II) concentrations, FeLume (II) measures radicals produced during the oxidation of Fe(II) at a high pH (≥ 11.0). Fe(II) is oxidized by dissolved molecular oxygen to produce superoxide and subsequently the peroxycarbonate radical. These species oxidize luminol in two steps to produce N₂ gas and light emission at 440 nm (Al-Gailani, Greenway and McCreedy, 2007). The system includes a glass spiral flow cell (FC) (Fig 2.8) and a PMT detector (Hamamatsu H9319) (Fig 2.9). Inside the FC, the Fe(II) standard or aerosol sample

solution and luminol reagent are mixed. The PMT detector is set perpendicular to measure the chemiluminescence reaction inside the FC. Both the PMT and FC are housed in a block (Fig 2.7 (d)) to prevent stray light from impacting the signal.

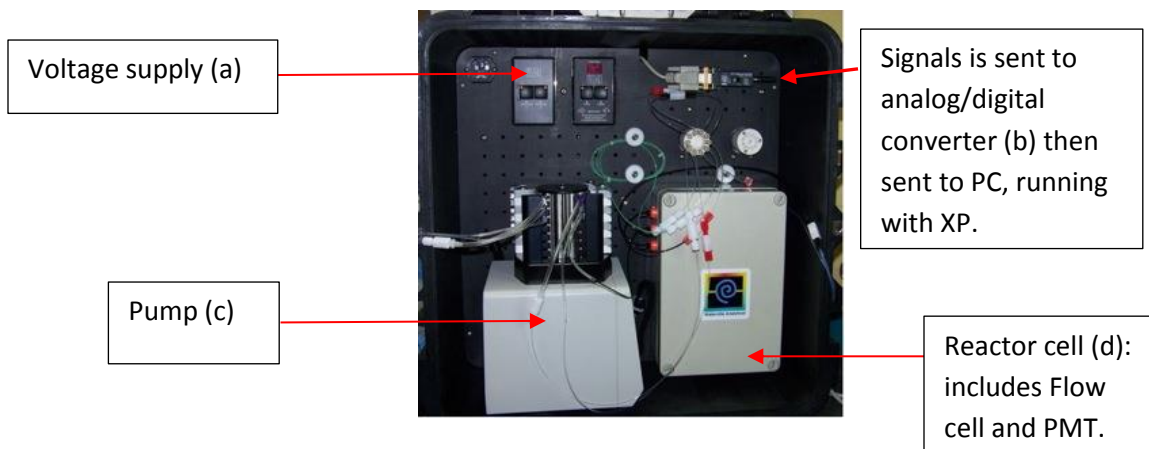


Figure 2.7 FeLume (II) system: (a) Input voltage is adjustable by using the RS-232 interface (Waterville Analytical) and controlled with a PC. The energy imparted by photons is passed to an interface module and converted to a readable format (b) that is sent to the PC. The peristaltic pump (c) provides consistent flow rate to distribute both Fe(II) solution/samples solutions and luminol reagent into the reactor cell (d) with Teflon tubes.

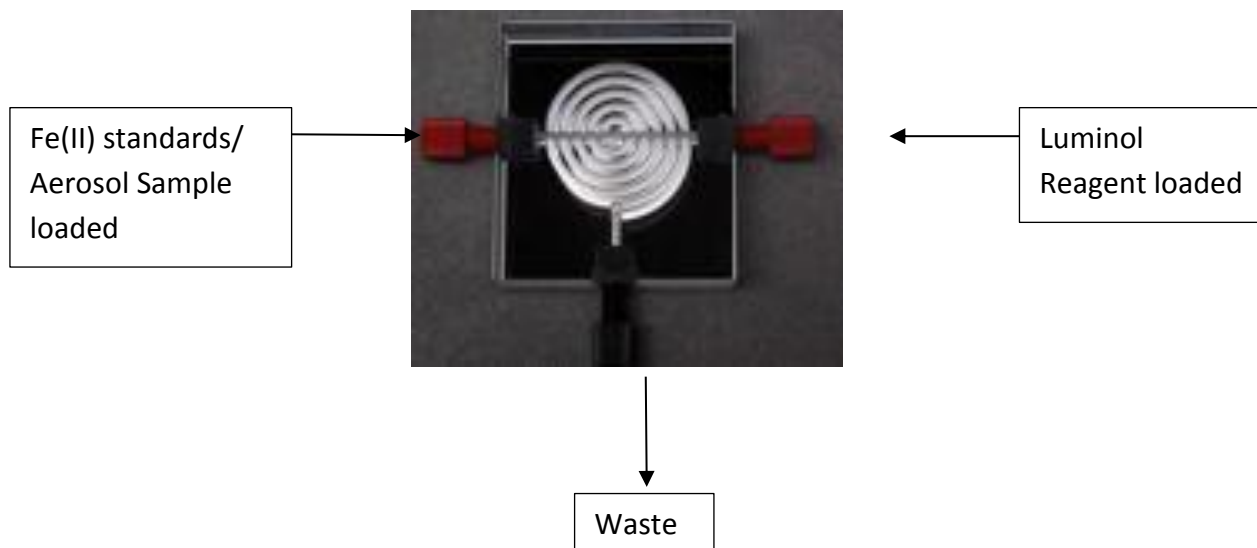


Figure 2.8 Flow Cell: An optical glass T-cell is housed inside a block with the PMT. Flow channels are 1 mm deep and 2 mm wide to provide uniform sample flow.



Figure 2.9 PMT: An integrated PMT module incorporating PMT detector, high-voltage supply, and photon counting circuitry. The PMT is vertically housed above of the flow cell to observe the light from the chemiluminescence reaction inside a box. The PMT module provides count linearity within a range of $\pm 1\%$ at $20 \times 10^6 \text{ s}^{-1}$ which is able to be controlled directly by an external computer through an RS-232 interface.

2.3.2.1 Luminol Reagent

A 0.1 mM luminol solution (Sigma-Aldrich, luminol 98%) was prepared in 1.0 M NH_3OH (Fisher Scientific, AR grade) based on a literature review (King et al. 1995) this solution needed to equilibrate for 24 hours and heated at 60°C for 16 hours in amber polypropylene brown bottles (Fisher Scientific). After the solution cooled to room temperature, the bottle needed to be uncapped and allowed to equilibrate with the atmosphere for 24 hours. In a final step, the pH was adjusted to 11.0 with concentrated NH_3OH (TraceMetal™ Grade, Fisher Scientific). This process provided the best stability and results. The solution was remade in anticipation of when it would be necessary.

2.3.2.2 Fe(II) Standard and Calibration

Three Fe(II) stock solutions, 4 mM, 40 μM , and 0.1 μM were prepared with ammonium iron(II) sulfate hexahydrate (Sigma-Aldrich, $\geq 99.9\%$ trace metals basis) in Nitrogen (N_2) purged Milli-Q water acidified to pH 2.2-2.5 with concentrated HCl (Fisher Scientific, trace metals basis). Prepared 4 mM Fe(II) solution was stored for a month, 40 μM was stored for one week, and the 0.1 μM Fe(II) solution had to be prepared freshly daily before using. The 0.1 μM Fe(II) solution was used to prepare standard solutions 10 pM- 2000 pM (Fig 2.9). Throughout the entire preparation process acid washed Teflon flasks or containers were used that were constantly rinsed with Milli-Q water between uses. A typical calibration curve is shown in Fig 2.10.

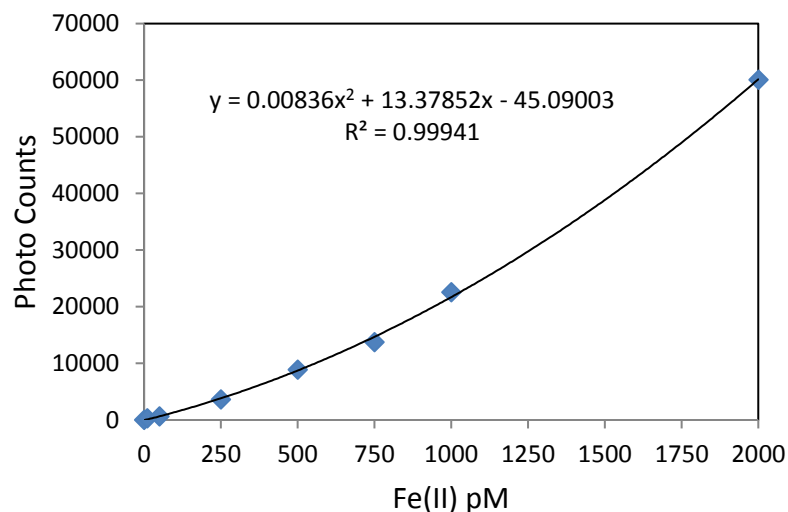


Figure 2.10 Photon counts as a function of the standard Fe(II) from 10pM – 2000pM, DL is 40 pM. The secondary order of equation is due to the chemical mechanism of the chemiluminescence reaction.

2.3.3 FIA-CL System for H₂O₂ Analysis

The FeLume (II) (Waterville Analytical) (Fig 2.7) was also used as an automated FIA system for the determination of H₂O₂ by detecting radicals released from the H₂O₂ with AE chemiluminescence reaction. Instead of directly determining the H₂O₂ concentrations, FeLume (II) measures radicals produced during the oxidation of AE which decays yielding N-methylacridone and light at pH ≥ 10.6 . AE is stable in acidic solution but will rapidly hydrolyze in a base and in the presence of the peroxide anion; AE forms an unstable dioxetane compound, which decays yielding N-methylacridone and light at a wavelength of 470 nm (King et al., 2007). The system works in the same way as described in the previous section for Fe(II) (2.3.2). To measure the H₂O₂ in

natural water, a second set of flow cell and detector were used for H₂O₂ analysis. The voltage was set at 900V for optimal signal and concentration ratio.

2.3.3.1 AE and Carbonate Buffer

To prepare the AE reagent solution, chemical AE (F.W. = 314.36) Reagent (Fig 2.5 [3]) had to be dissolved into Milli-Q water that had been treated with 3.0 mg L⁻¹ catalase (Sigma- from bovine liver) for at least 30 minutes in order to remove preexisting hydrogen peroxide in water. A stock 1.00 μM AE solution acidified with HCl to pH = 3.13 was prepared and kept in the fume hood. A diluted 80.0 nM AE reagent was prepared freshly to conduct the experiments each day.

Sodium carbonate buffer (Na₂CO₃) at pH= 11.0 (Fig 2.5 (4)) optimizes the detection sensitivity of the AE reaction with hydrogen peroxide. Buffer solution with both AE reagent and hydrogen peroxide should have a pH of around 10.6 for ideal results. The concentration of buffer depends on the type of sample. Here we used a 0.01 M Na₂CO₃ (Fluka, TraceSELECT ≥ 99.9%) solution that was prepared freshly before use. For the detection of hydrogen peroxide in pure water samples, a diluted buffer with 0.8 μM was used. For the detection of hydrogen peroxide in artificial seawater samples, a diluted buffer with 8.0 μM was used. For seawater samples, the 0.8 μM buffer was used and an additional 0.01 M HCl was used as a rinse agent for five minutes in between each experiment.

2.3.3.2 H₂O₂ Standards and Calibration

Three dilution series of stock H₂O₂ solutions, 0.1 mM, 5.0 μM, and 0.25 μM, were prepared freshly from Hydrogen Peroxide, 30% (Certified ACS, Fisher Chemical). The 0.25 μM H₂O₂ solution was used to prepare standard solutions 0.05 nM - 3.7 nM. A representative calibration curve is shown in Fig 2.12. All solution preparations were carried out using acid washed Teflon flasks/containers which were constantly rinsed with Milli-Q water prior to use and kept in the clean lab fume hood.

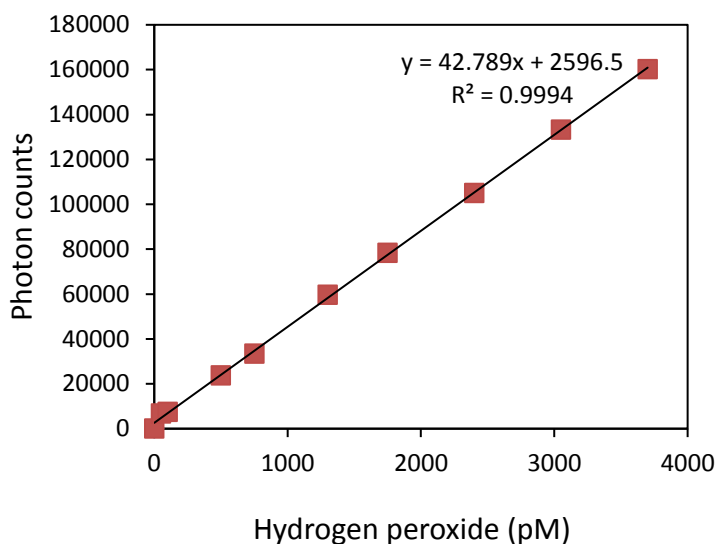


Figure 2.11 Photon counts as a function of the standard H₂O₂ from 0.05 nM - 3.7 nM. DL is 0.1 nM.

2.4 Solar Simulator

Sunlight was simulated with a 1000 W Xenon (Xe) O₃ free lamp in a fan-cooled housing (Thermo Oriel, Product Number 66921). The light was focused by a 2-inch diameter condensing lens inside the lamp housing that passed through a water-cooled

circulating IR chamber to remove excess heat. The light was then passed through two sequential air mass filters (AM 0+ AM1), which simulate the solar spectrum (Fig 2.8) at ground level of the equator when the sun is directly overhead. The beam turner, attached to the filter holder, directed the simulated sunlight at a 90° angle onto the reactor vessel. Experiments were carried out in a 50-mL Teflon flask with a quartz lid (Fig 2.6) as the cover.

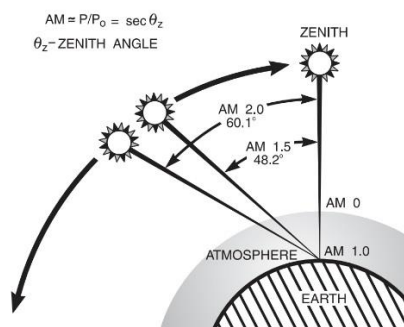


Figure 2.12 Path length in units of Air Mass, changes with the zenith angle. (Introduction to solar radiation, Newport)

2.5 Fe(II) concentration in Sampled Air Volume and Four Size Fractions

To obtain concentrations of soluble Fe in the air, photon counts were first converted to concentration (pM) by applying the Fe(II) calibration equation from the calibration curve (Eqn 3.1); this number Fe(pM) was the corrected for sample volume substrate fraction and air volume sampled (Fig 2.10). This resulted in a Fe(II) in air (ng m⁻³).

Eqn 3.1

$$Fe(pM) = -14.31 + \frac{-b + \sqrt{14.31^2 - 4(-0.008)(\text{Raw signal subtract blank})}}{2 * (-0.008)}$$

Eqn 3.2

$$\text{Total Fe}(ng\ m^{-3}) = \frac{Fe(pM)}{1000\left(\frac{ng}{pg}\right)} * 50\ (ml) * \frac{55.85\left(\frac{g}{mol}\right)}{1000\left(\frac{mL}{L}\right)} * \frac{1 / \text{fraction of substrate}}{\text{Air Volume Filtered}\ (m^3)}$$

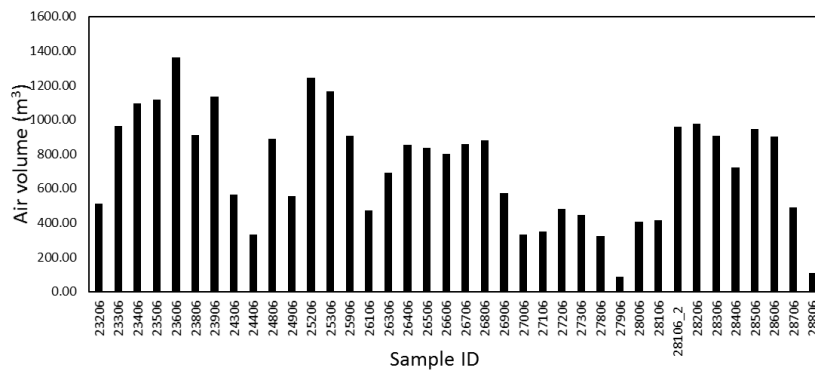


Figure. 2.13 Air volume (m³) pumped through each sample.

2.6 Volume Weighted Averages

North, central, and west - three distinct regions could be identified based on air mass back-trajectories (AMBTs). Volume weighted averaged concentrations for each region and overall in the following manner were computed.

$$Fe(II)\ (VWA) = \frac{\sum_i [Fe]_i * v_i}{\sum_i v_i}$$

CHAPTER III

RESULTS

In this chapter results from leaching experiments are presented. Raw data and absolute concentrations of Fe(II) are presented first, followed by the effect of added EDs in terms of rate of change in raw data and concentration of Fe(II). Subsequently, the initial Fe(II) released is compared to the preexisting concentration of EDs, which were determined by another graduate student (Lindsey Shank) in the past. Finally, the percentage of Fe(II) in total Fe is shown at the end of the results. In general, results for individual samples are presented first, then regional averages are computed and compared, and more detailed results are shown in the Appendix.

Hydrogen peroxide (H_2O_2) measurements showed all results to be below the detection limit (BDL) therefore they are not further discussed. Using the FIA-CL method, the DL of our method for H_2O_2 was 100 pM (Fig 2.10), which is lower than the currently reported H_2O_2 concentration in Pacific Ocean surface water of 10 to more than 250 nM (Yuan and Shiller, 2005). However, there were no significantly detectable signals of H_2O_2 during any of the simulation experiments.

3.1 Raw Fe(II) Data as a Function of Time

Raw Fe(II) results from two example leaching experiments are shown in (Fig 3.1). Photon counts were recorded every 0.33 seconds throughout the 285 second experiment. Each experiment includes five different stages as described in the method

section (Table 2.1). The 285 seconds of data collection was set to maximize the solution that could pass through the reactor cell while assuring completion of reaction, under the constraints of sample and reactor flask sizes and pump flow rate. Due to limited material, duplicate experiments could not be performed. Field blank data are subtracted from presented data. Note that light was turned on at 20 seconds, and that the observed effect of increased Fe(II) lags approximately by 25 seconds, as observed by the signal rise at about 45 seconds. This delay is representative of the time it takes for the solution to be pumped from the reactor vessel to the detector. A continued increase in signal was generally seen until the end of the experiment which included two ED additions. In general, the ultrafine size fraction displayed the highest signals (blue marker in Fig 3.1), while the large size fraction showed the lowest signals and generally no increasing trend (gray marker in Fig 3.1). The coarse and fine size fraction (yellow and orange markers in Fig 3.1) showed increased signals trend below the ultrafine and above the large size fraction.

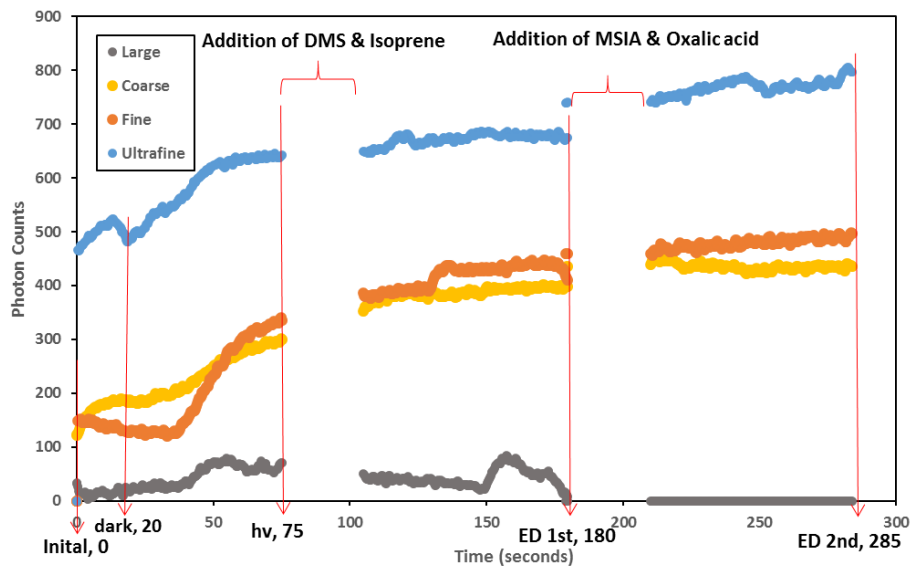
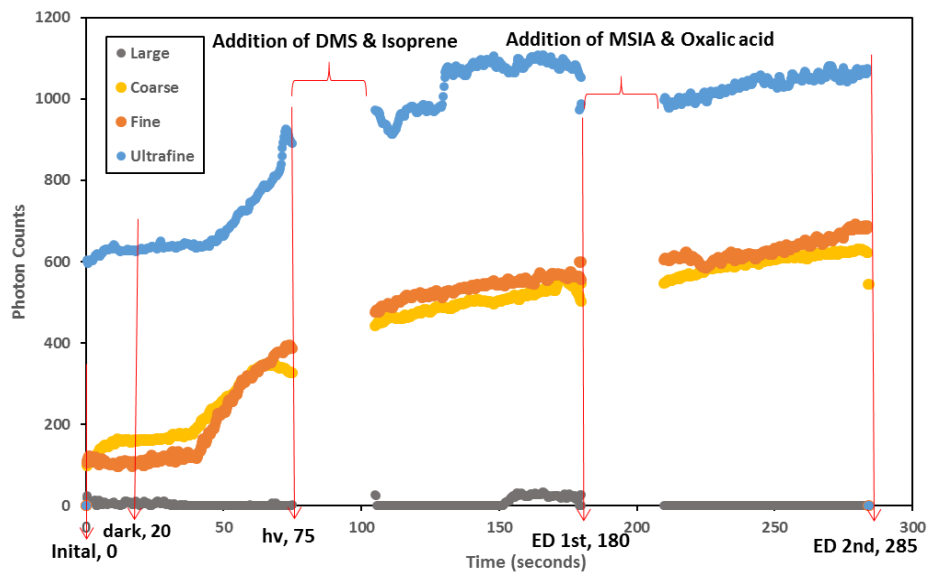


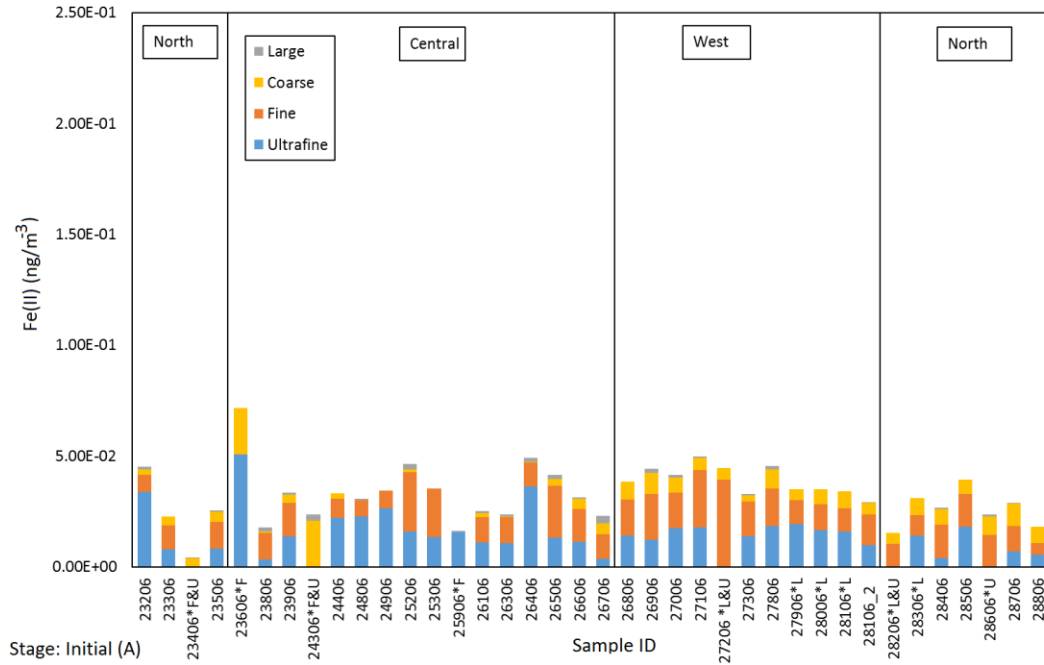
Figure. 3.1 Raw real-time results of photon counts for Fe(II) production of two example time sample sets as a function of time. Sample ID 23906 is at the top and 27006 is at the bottom. Red arrows point to the various stages as outlined in Table 2.1 [stage, time(s)].

3.2 Fe(II) Concentration in Sampled Air Volume and Four Size Fractions

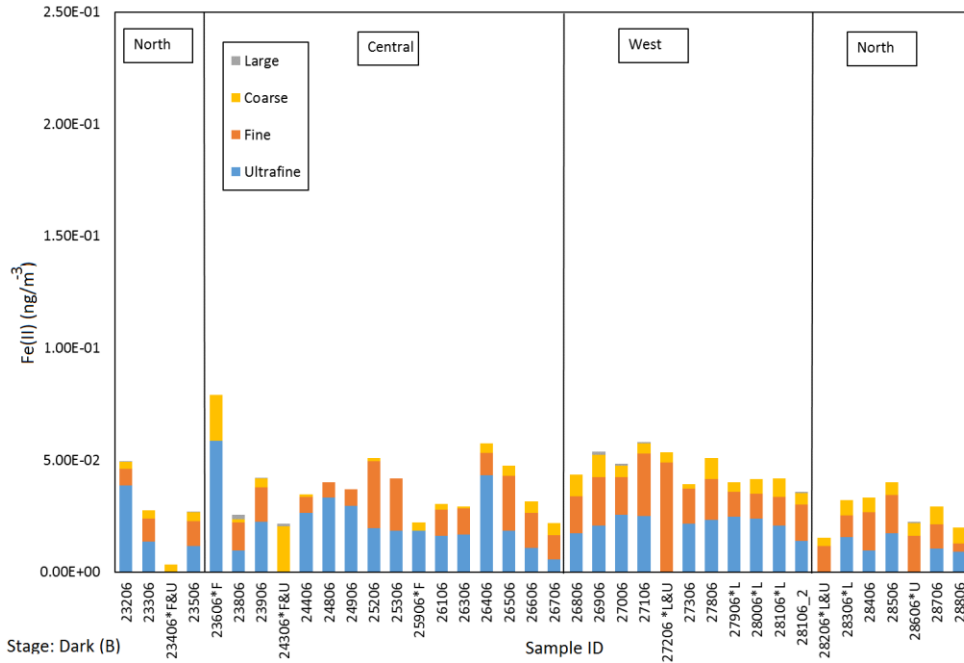
The 38 samples were collected from three regions along the equatorial Pacific Ocean. In each sample, the Fe(II) concentration of each size fraction was determined in pico-molar (pM) and converted to nano-gram per meter cube of air volume collected (ng m^{-3}) (See methods section 2.3.2.3). The concentration was determined at the end of the five stages as indicated by the red vertical lines in Fig 3.1. For reference, Fe(II) concentrations ranged from the DL (40 pM) to a maximum of 1.97 nM for all samples. Fe(II) concentrations in each sample and size fraction are presented in stacked bar graphs in Fig 3.2. From the top of the bar to bottom Fe(II) is contained in the large, coarse, fine and ultrafine size fractions. Of the 152 possible samples (38 samples X 4 substrates =152), the following were missing or BDL: In the large fraction, 6 substrates were missing and 8 substrates were BDL; in the coarse fraction, 3 substrates were BDL; in the fine fraction, 4 substrates were missing; and in the ultrafine fraction, 5 substrates were missing. Thus, of the 152 substrates, data for 15 samples were missing and for an additional 11 samples, results were BDL, representing 17% of samples. Results from each stage of extraction are presented in separate plots, Figs 3.2, A through E. In general, Fe(II) increased at every one of the five stages of the experiment, the large size fraction showed only small contributions throughout the five stages, and the ultrafine and fine fractions contributed the largest amounts.

Analogous but less obvious with the results from trace metal and ion analysis previously performed by other students, the data is divided into three distinct

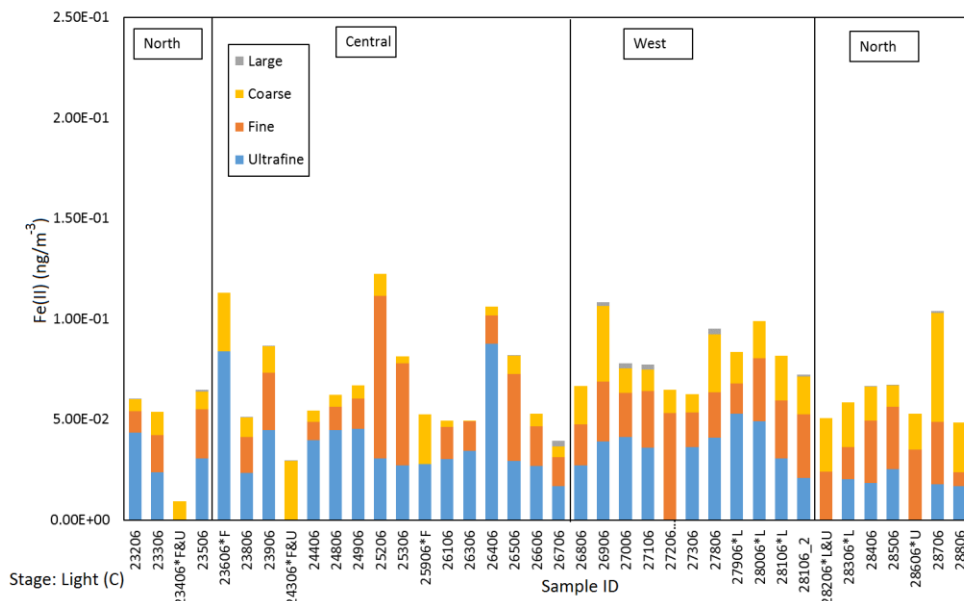
geographical regions: the northern, the central, and the western part of the cruise, as characterized by AMBTs. These are shown separated by vertical lines in Figs 3.2, A through E. Samples 23606-26706 fall into the central region, 26806-28106_2 into the west region, and 23206-23506; 28206-28806 into the north region.



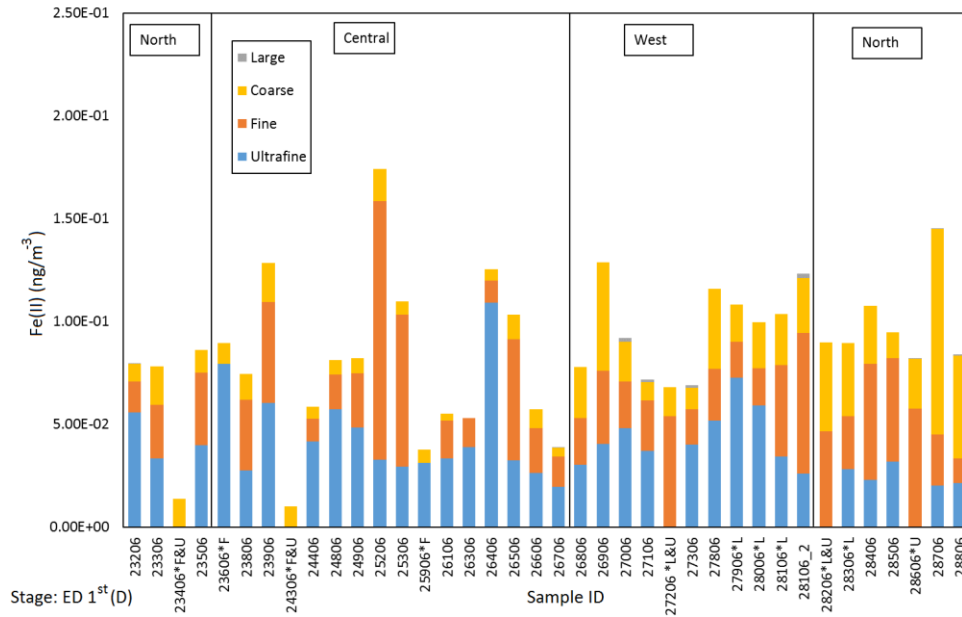
Figures 3.2 (A) Initial stage: Stacked bar plots of Fe(II) concentrations for each size fraction and sample at times 0 second. Fe(II) concentrations were determined in nano-gram per meter cube for each size fraction. Asterisk (*) notation, next to the sample ID indicates the size of fraction missing.



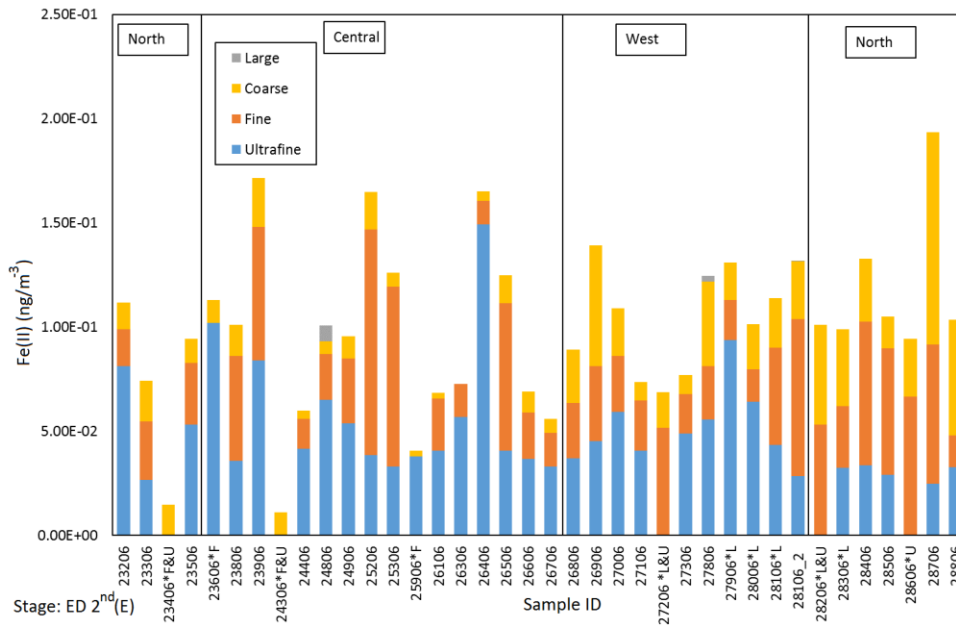
Figures 3.2 (B) Dark stage: Stacked bar plots of Fe(II) concentrations for each size fraction and sample at times 20 seconds.



Figures 3.2 (C) Light stage: Stacked bar plots of Fe(II) concentrations for each size fraction and sample at times 75 seconds.

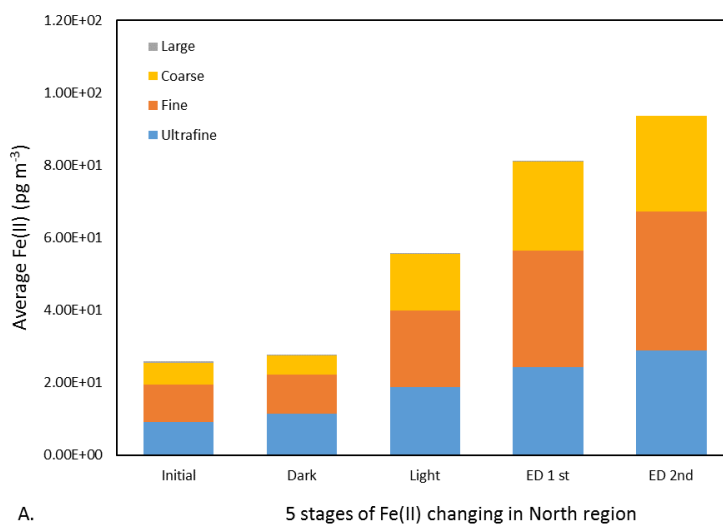


Figures 3.2 (D) ED 1st stage: Stacked bar plots of Fe(II) concentrations for each size fraction and sample at times 180 seconds.

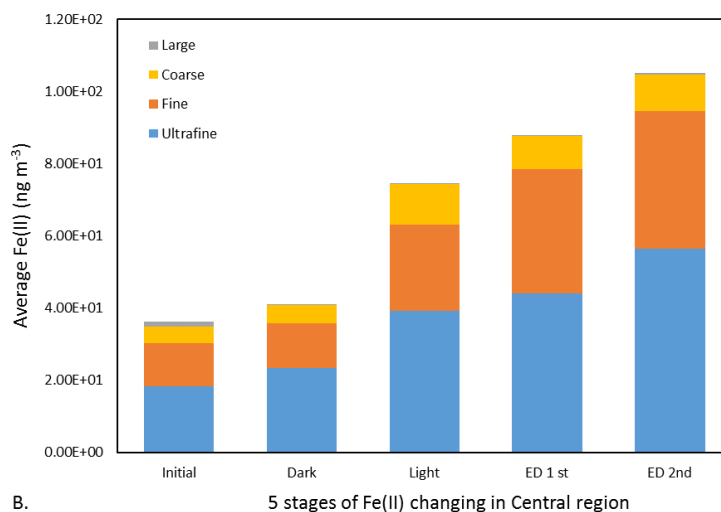


Figures 3.2 (E) ED 2nd stage: Stacked bar plots of Fe(II) concentrations for each size fraction and sample at times 285 seconds.

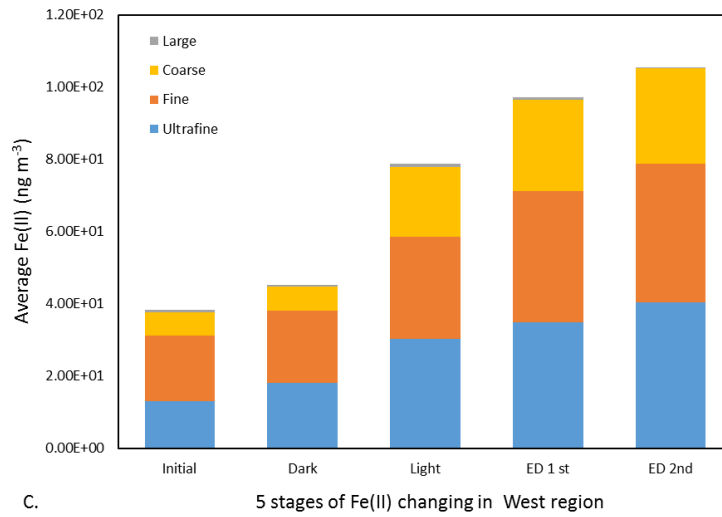
Volume weighted average atmospheric Fe(II) concentrations in all size fractions of each sample are presented in stacked bar plots which are representations of concentrations per region that are then used to determine significant differences between region and size fraction. To account for varying sample volumes, volume weighted averages are computed. For each region and overall, the average of Fe(II) in each fraction size is presented as Figs 3.3 A through D. The Fe(II) contribution from each filter size varied in each region. The relative contribution of Fe(II) released at the end of the experiments, representing the maximum, is shown in pie charts. UF-Fe has the largest average in the central region, 54%, fine Fe(II) is the next largest and relatively consistent across regions, compared to the west region, 38%, and North region, 31% (Fig 3.4). The absolute values of weighted averages for the maximum Fe(II) in each stage from fractions are listed in Appendix (Table A1). Observed Fe(II) concentrations were $0.29 \pm 1.48 \text{ pg m}^{-3}$ in large, $19.14 \pm 18.31 \text{ pg m}^{-3}$ in coarse, $38.80 \pm 37.87 \text{ pg m}^{-3}$ in fine, and $43.61 \pm 42.93 \text{ pg m}^{-3}$ in ultrafine size fractions – see Appendix (Table A1). Fe(II) sorted by regions are listed in Appendix (Table A2). To determine the relative ratios of initial, light, and ED stages, and if there are significant differences in between stages, regions and size fractions, Student's t-test were performed. P values are presented in Appendix (Table A3).



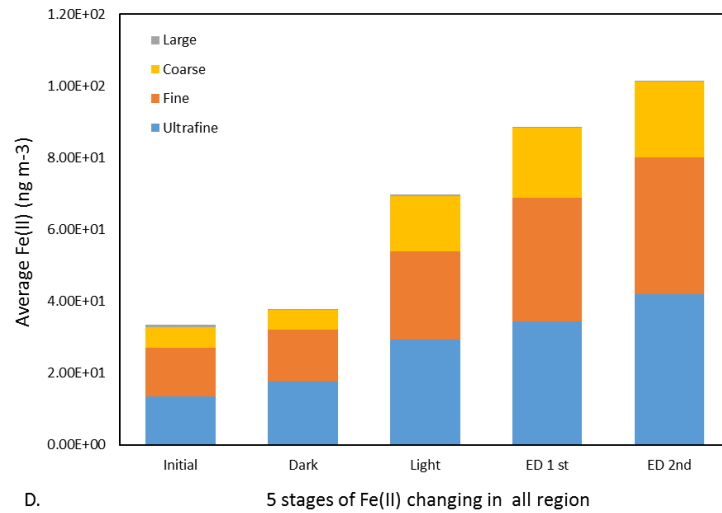
Figures 3.3 (A) Five stages of Fe(II) changes from initial to ED 2nd. In each bar, from top to bottom, different colors show maximum Fe(II) found in each size of samples. The results show sum of north region.



Figures 3.3 (B) Five stages of Fe(II) changes from initial to ED 2nd. The results show sum of central region.



Figures 3.3 (C) Five stages of Fe(II) changes from initial to ED 2nd. The results show sum of west region.



Figures 3.3 (D) Five stages of Fe(II) changes from initial to ED 2nd. The results show sum of all regions.



Figure 3.4 The volume weight average of Fe(II) in pg per m^{-3} contributed from each fraction of filters, at the end of reaction, are calculated in percentage in each region and overall.

3.3 Effect of ED Addition

To test the effect of EDs two sections of two fine samples were run - one without adding EDs and one with EDs (Fig 3.5). In both cases, it was apparent that after the first addition of ED, Fe(II) concentrations were significantly higher than without addition and that the second addition did not seem to make much of a difference. The relative increase in rate after the first ED addition was by 13.0% and 5.7%, and after the second

ED addition, it was by 1.0% and 1.2% for samples F28206 and F28506, respectively. The overall signal increase was by 20.9% and 13.8%, respectively, throughout the last 10 seconds of experiments. Due to limited sample material, we could not study this effect further in this way.

Instead, an attempt was made to find statistically significant changes between (i) light and ED1st, and (ii) ED1st and ED2nd stages by determining the slopes in the five seconds before and after EDs addition: before ED1st addition (a'a''), after ED1st addition (b'b''); before ED2nd addition (c'c''), and after ED2nd addition (d'd'') (Fig 3.6).

To visualize the ED effects on the Fe(II) formation rate, the slopes a'- a'', b'- b'', c'- c'' and d'- d'' are presented in Appendix (Figures A1 A-F) for the coarse, fine, and ultrafine size fractions. Since Fe(II) in the large size fraction did not show significant changes, it is not shown. To compare the rates before and after ED additions, a'a'' is plotted with b'b'', and c'c'' is plotted with d'd''. In general, between light to ED1st the reaction rate seemed to decrease while between ED1st to ED2nd the reaction rate increased in all size fractions.

Overall rates are smallest in the ultrafine size fraction and largest in the fine fraction. To establish regional patterns, volume weighted averages were computed analogously as performed for concentration in the previous section. These are presented in Fig 3.7. In general, the rate of changes of Fe(II) is lower during the ED1st but larger during the ED2nd in both coarse and fine size fractions, and there is no significant difference in between ED1st to ED2nd in ultrafine fraction. Student's t-test was used to

identify significant differences in volume weighted averages between stages and results are presented in Table 3.1. In general, there were significant differences between ED1st to ED2nd in all size fractions. There were significant differences between light to ED1st in coarse and fine size fractions.

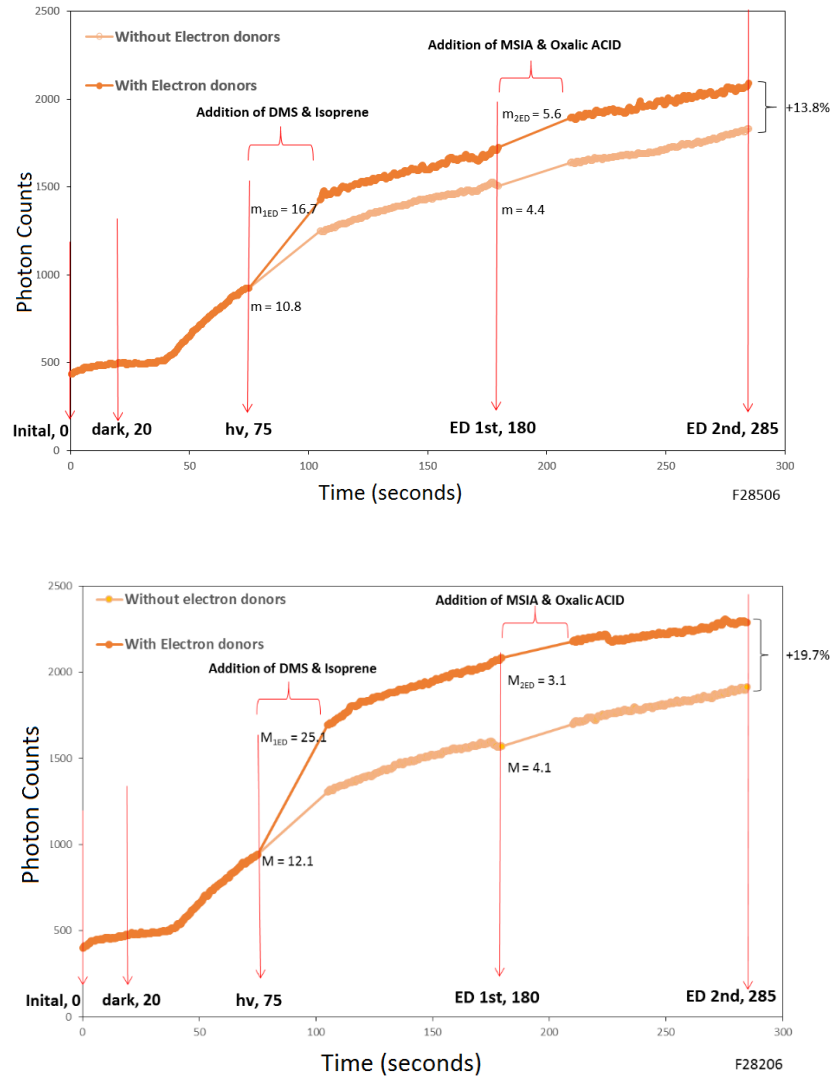


Figure 3.5 Photon counts vs. time for fine fraction of samples 28206 (top) and 28506 (bottom). Dark orange represents data with ED addition, while the light orange is data

from a different section of the same sample run without ED addition. The slopes with ED are defined as M_{1ED} and M_{2ED} .

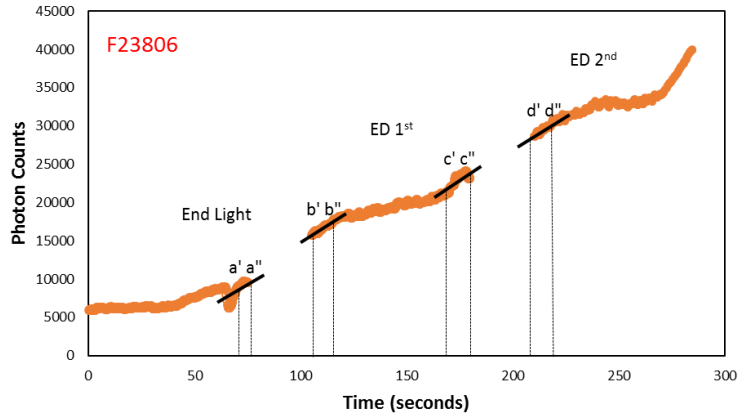
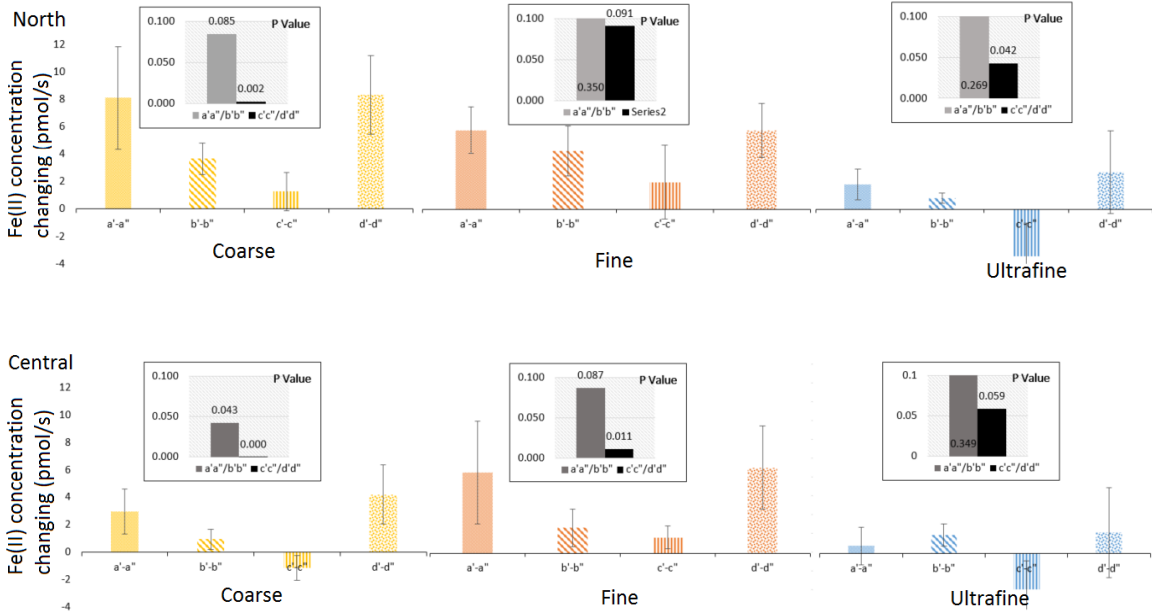


Figure 3.6 An example (Fine sample 23806) of slope determination at the various stages: the last 5 seconds of the light reaction (a' - a''), first and last 5 seconds of $ED1^{st}$ (b' - b'' ; c' - c'') and first 5 seconds of $ED2^{nd}$ (d' - d'') reaction.



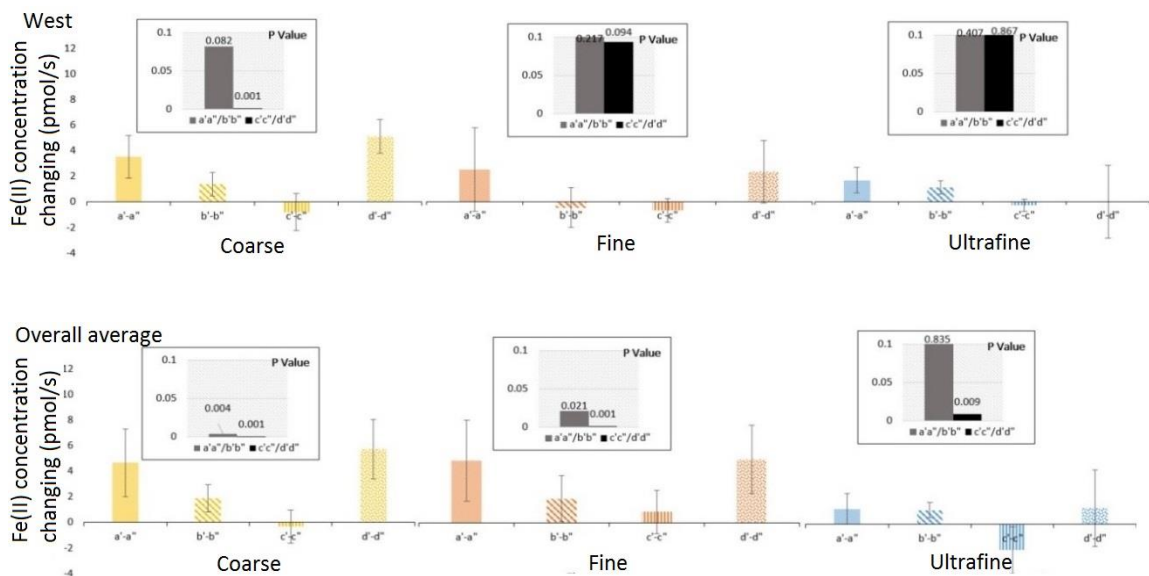


Figure 3.7 Regional and overall average of Fe(II) production rate changes with P value for significant differences before vs. after addition of ED1st (gray) and ED2nd (black).

Table 3.1 T-test of deviation from slope to slope using two-sample, assume equal variance in 0.5 (pmol per second).

Size of fraction (# samples)	Mean of slopes (pmol/s)					
	a'-a''	b'-b''	p value	c'-c''	d'-d''	p value
coarse (36)	4.75	1.90	*	-0.29	5.65	***
fine (34)	5.08	1.92	*	0.76	5.08	***
ultrafine (32)	1.28	1.10	p > 0.05	-2.10	0.83	**

*significant at p < 0.05; ** significant at p < 0.005; *** significant at p < 0.001

3.4 Initial Fe(II) Concentrations in Relation to Naturally Present EDs

Presented above are results for Fe(II) production in context of added EDs. Here, the initial Fe(II) concentrations are compared to EDs that were already present on the substrates. These had been determined by previous graduate student, Lindsey Shank. This is done to investigate whether pre-existing EDs or products thereof had a significant impact on Fe(II) formation in the initial stage. To that end, initial Fe(II) concentrations are compared with detected EDs, including oxalate and malonate. EDs oxidation products, including MSA and NSS-sulfate, and as well as total Fe are also included in the analysis. EDs were analyzed with ion chromatograph (IC) and total Fe with inductively coupled plasma mass spectrometry (ICP-MS). Correlation matrices and linear regression plots were investigated by region. Due to the complex nature of these sample, correlation coefficients of $R^2 > 0.2$ were deemed significant enough to investigate further in a multivariate linear regression analysis. Relationships were found most pronounced between Fe(II)-dark with NSS-sulfate, and Fe(II)-light with malonate and total Fe. The strongest correlations are presented in regression plots for visual inspection in the Appendix (Figures A2 A-L) and the result is summarized in the Appendix (Table A4).

The approach for modeling the relationship between Fe(II) concentration and EDs was attempted using multivariable linear regression analysis on the entire data set with SPSS software to try and predict the value of the dependent variable, i.e. FIA Fe(II). Independent variables were selected based on the positive correlations found with Fe(II)

which included Fe_{tot} , malonate, oxalate, MSA and $NSS-SO_4^{2-}$. The following equation was used to generate coefficients, in addition to parameters (P and R^2 values), that describe the validity of the data with our hypothesized model.

$$\text{Eqn 3.1} \quad [Fe(II)] = a[Fe_{tot}] + b [MSA] + c[Mal] + d[Oxa] + e[nss - SO_4^{2-}] + f$$

Standardized coefficients are presented in bars in Fig 3.8. This value provides a measure of the normalized magnitude that each coefficient contributes to Fe(II). The value of R^2 is a measure of the percent variance in the data that the model describes and significance is how well the overall analysis describes the dependent variable, significantly smaller than 0.08 is good in this case. Each parameter also has a P value cited with it that describes how significant its contribution is. When that P value is smaller than 0.08, the associated box is outlined in red. Note that ultrafine samples are not shown on the graph due to insufficient IC data. In general, $NSS-SO_4^{2-}$ seemed to contribute positively to Fe(II) formation while malonate and MSA played a negative roll with Fe(II). In addition, total Fe contributed positively in the fine and coarse fractions and consistently negative in the large fraction.



Figure 3.8 Results from multivariate regression analysis are presented in bar graph. Each bar is the value of the standardized coefficients.

3.5 Percent (%) Fe(II)

To better understand the relationship between Fe(II) and total Fe in surface waters, concentrations of both were measured from the same set of samples. From previous work (Lindsey Shank), total Fe was determined in each size fraction of all samples (Fig 4.2) using the ICP-MS method. The percentage of Fe(II) concentration determined with FIA-CL method is calculated and shown in the Appendix (Figures A3 A-D and Figures A4 A-D).

3.5.3 Regional and Overall Fe(II) of Total Fe

It appears that relative Fe(II) released from the fine fraction is the largest when compared to large, coarse and ultrafine. To show this distribution and also compare between regions, volume weighted average percentages of Fe(II) in respective size fractions were determined for each stage and presented in stacked bar plots for all size fractions and regions (Fig 3.9). It is apparent that the percentage of Fe(II) in the fine size fraction is significantly larger in all regions and overall. Furthermore, light and ED addition showed the largest contribution in the north and central regions, while initially Fe(II) was the predominant component in the west. This could be explained by the larger anthropogenic contribution of organic acids already having processed Fe in the western region. Adding all size fractions together, Fe(II) was found in a concentration of less than 3% of total Fe. The contribution of each from high to low is in the order of fine, coarse, ultrafine, and large. The percentage Fe(II) contribution in fine size fraction by region is in the order of north, central and west region.

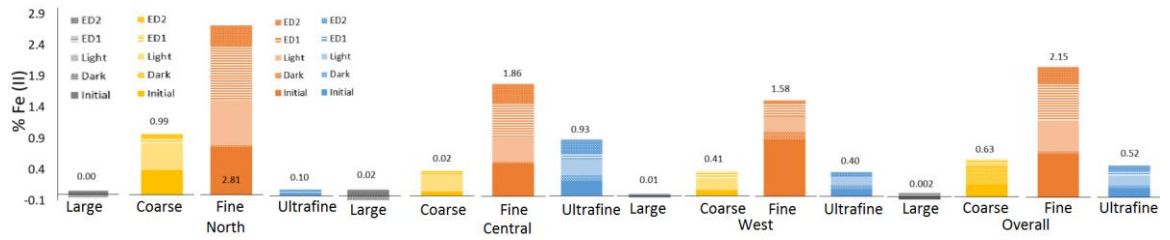


Figure 3.9 Regional and overall % Fe, all size fraction stacked bar graph. % Fe is calculated by volume weight average.

CHAPTER IV

DISCUSSION

The focus of this thesis is to determine the distribution of atmospheric Fe(II) in sampled regions over the equatorial Pacific Ocean and to investigate chemical mechanisms that control Fe(II) concentrations once deposited into the ocean. Of particular interest are the characteristics of the various aerosol size fractions, the role of organic ligands, and the geographical variability across the three different sampled regions.

4.1 Bioavailable Fe Concentrations in Aerosols and in Simulated Surface Water over the Equatorial Pacific Ocean

The concentrations of Fe(II) in aerosols were determined in samples collected in a triangular region southwest and southeast of the Hawaiian Islands in the equatorial Pacific Ocean, where the Hawaiian Islands are the apex of the triangle. Observed Fe(II) concentrations were $0.29 \pm 1.48 \text{ pg m}^{-3}$ in large, $19.14 \pm 18.31 \text{ pg m}^{-3}$ in coarse, $38.80 \pm 37.87 \text{ pg m}^{-3}$ in fine, and $43.61 \pm 42.93 \text{ pg m}^{-3}$ in ultrafine size fractions, see Appendix (Table A1). Dissolved Fe(II) in the atmosphere has been measured over several oceanic regions, including the Indian, Atlantic, Pacific and Southern Oceans (Table 4.1). However, there is little data on dissolved Fe(II) concentrations from aerosols in the equatorial Pacific Ocean. Results from this study were generally comparable to those of other marine environments, especially the analysis conducted over remote ocean regions. In accordance with our prediction, the highest total dissolved Fe(II)

concentrations found through our research were lower than other similar studies, such as over the Northwest Pacific Ocean, where there were large amounts of dust highly contaminated with anthropogenic air pollutants.

Table 4.1 Comparison of Fe(II) and total Fe (Fe_{tot}) atmospheric aerosol concentrations in different regions.

Locations	Fe(II) ($ng\ m^{-3}$)	Fe_{tot} ($ng\ m^{-3}$)	Citations
Northwest Pacific	0.05–5.3	0.28–86	Buck et al. (2006)
East China Sea		1.7–120	Hsu et al. (2009)
North Atlantic	2.5 ± 1.8 (0.63–8.2)	12 ± 8.4 (2.8–33)	Zhu et al. (1997)
North Atlantic	0.19–1.2	0.35–20	Chen and Siefert (2004)
North Atlantic		4.5–12	Sedwick et al. (2007)
North Atlantic	4.28 ± 3.42	840 ± 610	(Hoffmann, Siefert and Johansen, 2000)
North Indian Ocean	0.13 ± 0.017	9.8 ± 3.4 (3.9 - 17.2)	(Hoffmann and Johansen, 2003)
Coastal East Antarctic	0.53 ± 0.38 (0.18–1.3)	1.2 ± 1.1 (0.23–3.3)	Gao et al. (2013)
US Northeast Coast	2.1	2.4	Xu and Yuan Gao (2017)
Newark	(1.2–4.2)	(1.3–4.9)	
Equatorial Pacific	$0.29E-3 \pm$	36.67 ± 82.49	This study;
Ocean	$1.48E-3 \sim$		(Lindsey Shank)

4.2 Fe(II) Distribution as a Function of Aerosol Size and Region

Aeolian Fe deposition is the major source of Fe(II) in the remote regions of the ocean studied, and evidence shows that the bulk of atmospherically derived dissolved Fe is most commonly found in the form of colloidal (0.02-0.4 μm) pools and not truly dissolved (<0.02 μm) pools (Bergquist, Wu and Boyle, 2007). The results from experiments on the dissolution of aerosol Fe in seawater leaching (Aguilar-Islas et al., 2010) confirmed the colloidal size which contributed most dissolved Fe to the ocean's surface. Samples analyzed in the Aguilar-Islas' study were collected alongside the samples used in the present study.

When looking at the relative distribution of the maximum extractable Fe(II) (after ED2nd) amongst the four aerosol size fractions, the ultrafine fraction ($d_a < 0.1 \mu\text{m}$) contributed 31-54%, the fine fraction ($0.1 \mu\text{m} \leq d_a < 1 \mu\text{m}$) contributed 36-41% of Fe(II), and the coarse fraction ($1 \mu\text{m} \leq d_a < 10 \mu\text{m}$) contributed 10-28% of Fe(II). Fe(II) in the large fraction was below 1% (Fig 3.4). The percentage of Fe(II) to total Fe, followed a similar pattern: 2.15% in the fine, 0.63% in the coarse, 0.52% in the ultrafine, and 0.002% in the large fraction (Fig 3.9).

Each size fraction seems to be behaving differently in terms of Fe(II) concentrations when compared to the total available Fe. In the ultrafine, significant amounts of total Fe were not reduced, even after the addition of light and ED, as compared to the other size fractions. This may indicate a refractory fraction of Fe that is

solely present in nanometer sized particles. In addition, organic anions detected with the IC and known to promote reductive Fe dissolution, were not as concentrated in ultrafine size fraction compared to the other size fractions (Fig 4.1)

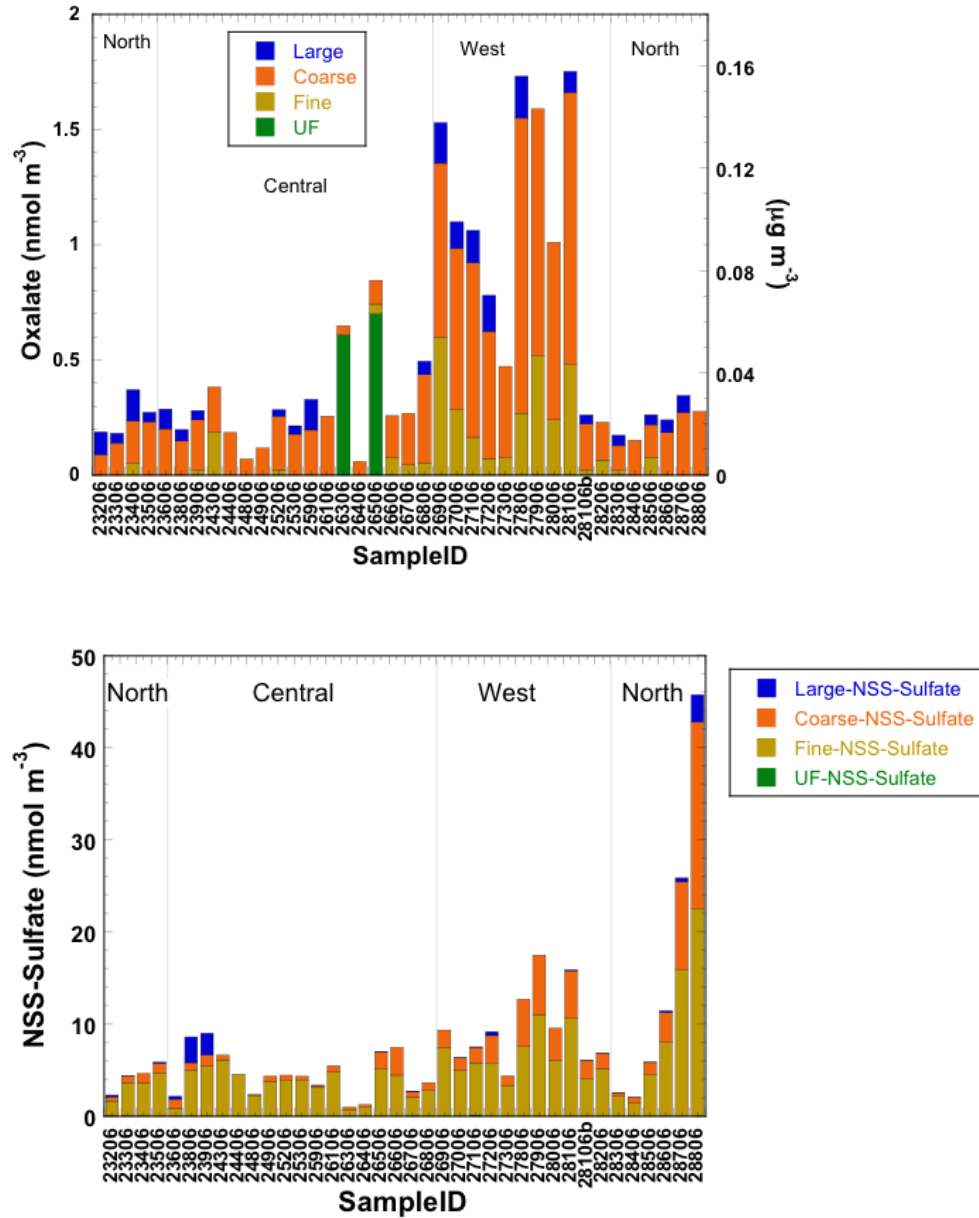


Figure 4.1 Organic anions, oxalate and NSS-SO₄²⁻ detected with the IC analyzing the same set of samples.

Fe(II) concentration in the ultrafine fraction from the central region showed there were significant differences (p value < 0.05) comparing with the ultrafine sample from the north region in initial, light, and ED2nd stages, see Appendix (Table A3, bottom). However, while comparing Fe(II) production rate in both ED1st and ED2nd stages showed no significant changes from ultrafine fraction in both north and central regions (Fig 3.7). That is, EDs addition to ultrafine fraction was not showing significant impacts to alter Fe(II) production rates in the stimulation experiment. Since the Fe(II) concentrations showed significant difference in the three stages, it can be concluded that there were different chemical components compared to the north and central regions' samples. Initially, the central region seemed to contain double the amount of Fe(II) compared to the north (2 fold); however, after the light stage, samples from the north released more Fe(II) than those from the central region (1.2 fold) – Also see Appendix (Table A3, top). This could be attributed to the larger presence of organic acids in samples from the north. After ED2nd, the central region contained more Fe(II) again (2 fold). It proved that there were Fe(III) species preexisting in an ultrafine size fraction. This Fe(III) species was less likely to be photolyzed but could form Fe(III) ligands with EDs, such as oxalate or MSIA. Since from our data analysis, Fe(II) production rates were not showing significant differences through the ED1st to the end which indicates that the possible preexisting Fe (III) species were found in very few samples collected in ultrafine fraction in the central region.

There was significant difference between the north to west regions in fine fraction but only in the initial stage, and Fe(II) concentration was about doubled in the

western region - See Appendix (Table A3). The significant difference of Fe(II) concentrations was not seen in any other stages since samples from the western region contained the most anthropogenic air pollutants in the fine fraction which already reduce Fe(III) in the aerosol sample before the simulation experiment was performed.

There was a significant difference between the central to west region in coarse fraction in light and ED2nd stages. Fe(II) concentration was approximately double in the west region at light stage but 2.62-fold in central after ED2nd - See Appendix (Table A3). This indicates that there was little Fe(II) in the coarse particles in the central region, but significant Fe(III) that was then able to be reduced when exposed to ED2nd (Fig 3.7, central).

4.3 Chemistry of Fe(II) Dissolution

4.3.1 Photochemical Dissolution

The reduction and oxidation of Fe can occur through a number of processes. These processes include direct mediation through the photochemical reduction of colloidal iron (Waite & Morel, 1984) or Fe(III)-organic ligand complexes (Barbeau et al., 2001, 2003). Except for large size fraction ($p > 0.05$), all fractions showed significant increased Fe(II) concentrations in the light stage (Fig 3.1). This could be a consequence of the existence of Fe(III) species and/or organic compounds promoting photochemical dissolution due to their pre-existence in the fine, coarse, and ultrafine size particles where there is lower percentages of Fe(III) ligands in the large fraction.

4.3.2 Electron Donors Impact on Fe Reduction

ED1st - DMS and Isoprene: So far there is no direct evidence of the impact of DMS or isoprene to photochemical Fe dissolution, and the roles of both are still unclear. Much research has found isoprene as having a positive correlation of measured photosynthetic capacity in ocean surface water and suggested isoprene production (~4.8 Tg C per year) is closely related to phytoplankton activity (Srikanta Dani et al., 2017). The importance of isoprene was supported by high concentrations of isoprene over the remote marine atmosphere found to be up to 280 parts per trillion by volume over the Southern ocean (Yokouchi et al., 1999). However, it was found that isoprene appears to be an insignificant source of organic carbon in the remote marine atmosphere, contributing only about 2% of organic aerosol yield (Arnold et al., 2009). Our results indicate the rate of Fe(II) production was not increased significantly due to the addition of DMS and isoprene (Table 3.1). However, in the two sample sections where both the addition and absence of ED1st were compared, the immediate results seemed to be that of an enhanced production of Fe(II) (Fig 3.5).

ED2nd - MSIA and Oxalate acid: A positive linear correlation between Fe solubility and oxalate concentration was found (Paris, Desboeufs and Journet, 2011) in the same study, where soluble Fe concentrations increased from $0.0025\% \pm 0.0005\%$ to $0.26\% \pm 0.01\%$ of total Fe with the presence of aeolian dust sources and also with oxalate concentrations ranging from 0 to 8 μM from the aerosols collected over the Atlantic Ocean (Paris, Desboeufs and Journet, 2011). In a module-predicted calculation, oxalate-

promoted Fe dissolution led to ~75% increase in Fe_d deposition to the ocean (Johnson and Meskhidze, 2013). In our results, MSIA and oxalate acid addition was found to promote the Fe dissolution rate in coarse, fine, and ultrafine size fraction (Fig 3.5 c'c''/d'd''; Table 3.1), likely through the formation of organic ligands and promoting Fe dissolution (Johansen and Key, 2006). While compared with ED1st, the addition of ED2nd, MSIA and oxalate, promoted Fe(II) concentrations in both coarse and fine fractions sample by 7.64 to 11.91 %, respectively (Fig 3.7).

4.4 Fe(II) Dissolution as Function of Naturally Present EDs

In our study, initial Fe(II) concentrations were found to have positive linear correlation to both oxalate (west region, all size fractions) and malonate (central region, coarse; west region, fine). However, after being exposed to light, a positive linear correlation also arose with oxalate (central region, coarse) and malonate (west region, ultrafine). Initial Fe(II) concentrations were also found to have a positive linear correlation to NSS-SO₄²⁻ (central region, fine); and total Fe (north region, coarse). After exposure to light, Fe(II) concentration increased and had a positive linear correlation to NSS-SO₄²⁻ (north region, fine; central region, fine), MSA (north region, fine; central region, coarse) and total Fe (north region, ultrafine) – See all in Appendix (Figures A2 A-L). It also suggests that these preexisting organic compounds possibly promote Fe(III) dissolution. However, with the above findings, that organic matter correlated with Fe(II) concentrations, we took further steps to investigate using a multivariable linear regression to try and describe the Fe(II) concentrations (Fig 3.8). The results showed

some different correlations, that only oxalate, NSS-SO_4^{2-} and the total Fe showed significant positive contributions to the Fe(II), and MSA and malonate showed significant negative contributions to the Fe(II). Although we showed the case of positively correlating results in the Appendix (Figures A2 A-L), there are also negatively correlated results not presented here.

Recent research compared the photoreactivities of Fe(III)-Oxalato and Fe(III)-Malonate complexes in a UV/Fe(III) system and found that although both oxalate and malonate were able to form Fe(III) ligands leading to the photochemical reduction of Fe(II), the Fe(III)-malonate complex generated relatively low Fe(II) concentrations through photolysis compared to the well-known reactivity of oxalate complexes (Xiao et al., 2014). In this study, the concentration of organic compounds were investigated at different magnitudes and compared with Xiao's study (pM vs. μM). Our work, at this stage, agrees with the results from Xiao, suggesting that preexisting organic compounds, oxalate, potentially promote the forming of Fe(III) complexes and then proceed to Fe dissolution and have the opposite effect with malonate. The negative standard coefficient in Fig 3.8 of MSA and malonate could also be caused by preexisting organic matter reacting with luminol radicals and thereby suppressing the photo count signal results (Pullin and Cabaniss, 2001; Rose and Waite, 2001). This result could be supported using Gaussian[®] 09 program to calculate the thermodynamic stability of the chemical system. In this case, the energy difference of reduction of Fe(III)-Oxalato and Fe(III)-Malonate ligand complexes to Fe(II) ligand complexes were computed. The

results (Communication with Dr. Yingbin Ge) showed that the reduction of Fe(III) to Fe(II) is more favored thermodynamically by 20 kJ/mol if oxalate is the ligand.

4.5 Percentage of Fe(II) to Total Fe

In the remote ocean's surface, the data of the percentage of Fe(II) to total Fe was investigated and reported in many studies. In a recent study, aerosol solubility in the same ocean areas was investigated through collected aerosol samples; the median fractional solubility of aerosol Fe was 9.2% in ultrapure water and 6.4% in seawater. On average, 0.195 pg m^{-3} of Fe(II) which accounted for 1.7% of the total aerosol Fe and 26.2% of the seawater soluble aerosol Fe (Buck, Landing and Resing, 2013). Aerosol Fe dissolution in the Northern Pacific oceanic waters was determined with batch-leaching methods. Seawater-dissolvable labile aerosol Fe was found at $5.7 \pm 2.0\%$ of total Fe (Aguilar-Islas et al., 2010). Over the equatorial Pacific Ocean, the percentage of Fe(II) of total Fe (Fig 4.2) was investigated in this study. The percentage of Fe was found from 1.58-2.81% and 2.15% in average in fine size fraction; 0.02-0.99% and 0.63 % in average in coarse fraction; 0.10-0.93% and 0.52% in average in ultrafine fraction (Fig 3.9).

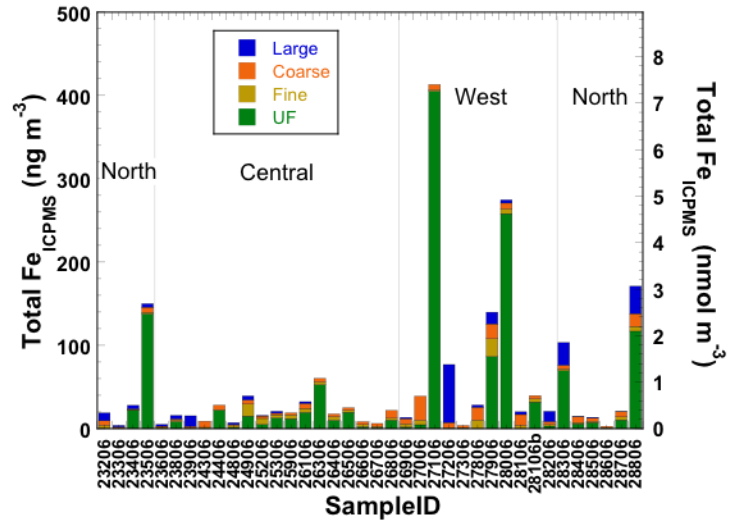


Figure 4.2 Total Fe from each fraction using ICP-MS.

CHAPTER V

CONCLUSION

Fe(II) in aerosols was generally found in coarse, fine, and ultrafine size but very small amounts in the large. The concentrations of Fe(II) in aerosols of the various size fractions were found to be: $0.29 \pm 1.48 \text{ pg m}^{-3}$ in large, $19.14 \pm 18.31 \text{ pg m}^{-3}$ in coarse, $38.80 \pm 37.87 \text{ pg m}^{-3}$ in fine, and $43.61 \pm 42.93 \text{ pg m}^{-3}$ in ultrafine samples. Fe(II) distribution from varying regions shows significant differences likely due to the source of the aerosol iron and the different chemical components. The percentage of Fe(II) in the fine size fraction is significantly greater in all regions. Light and ED addition showed the largest contribution in samples from the north and central regions, while the initial Fe(II) was the predominant component in the western region. In all size fractions together, the Fe(II) concentration in total Fe was less than 3%.

Photochemically induced Fe dissolution was confirmed in coarse, fine, and ultrafine size fractions. There was a significant increase with DMS and isoprene in the two sample sections used; however, the change in Fe(II) production rate was not significant. MSIA and oxalic acid showed significant increase in Fe(II) dissolution after addition.

Originally present malonate, oxalate, and NSS-SO_4^{2-} were found to have positive correlations with Fe(II) concentrations in both the dark and light stages in the experiments. However, in the multivariable linear regression analysis, in general, oxalate and NSS-SO_4^{2-} seemed to contribute positively to Fe(II) formation while malonate and

MSA had a negative impact on Fe(II) formation. In addition, total Fe contributed positively in the fine and coarse fractions and consistently negative in the large fraction.

In conducting this research our methods, at the time, differed from others due to the equipment utilized, namely the FIA-CL detection, which allowed us to lower the detection limits to pico-molar concentrations in a neutral medium which was not a common method applied to such investigations. Necessary advances in analysis equipment will further help develop the understanding of Fe(II) dissolution in seawater.

REFERENCES

- Aguilar-Islas, A., Wu, J., Rember, R., Johansen, A. and Shank, L. (2010). Dissolution of aerosol-derived iron in seawater: Leach solution chemistry, aerosol type, and colloidal iron fraction. *Marine Chemistry*, 120(1-4), pp.25-33.
- Al-Gailani, B., Greenway, G. and Mccreeedy, T. (2007). A miniaturized flow-injection analysis (μ FIA) system with on-line chemiluminescence detection for the determination of iron in estuarine water. *International Journal of Environmental Analytical Chemistry*, 87(9), pp.637-646.
- Arakaki, T. and Faust, B. (1998). Sources, sinks, and mechanisms of hydroxyl radical (\bullet OH) photoproduction and consumption in authentic acidic continental cloud waters from Whiteface Mountain, New York: The role of the Fe(r) (r = II, III) photochemical cycle. *Journal of Geophysical Research: Atmospheres*, 103(D3), pp.3487-3504.
- Arnold, S., Spracklen, D., Williams, J., Yassaa, N., Sciare, J., Bonsang, B., Gros, V., Peeken, I., Lewis, A., Alvain, S. and Moulin, C. (2009). Evaluation of the global oceanic isoprene source and its impacts on marine organic carbon aerosol. *Atmospheric Chemistry and Physics*, 9(4), pp.1253-1262.
- Aumann, E. and Tabazadeh, A. (2008). Rate of organic film formation and oxidation on aqueous drops. *Journal of Geophysical Research*, 113(D23).
- Barbeau, K. (2006). Photochemistry of organic iron(III) Complexing ligands in Oceanic systems. *Photochemistry and Photobiology*, 82(6), p.1505.
- Barbeau, K., Selph, K. and Buck, K. (2010). Iron-binding ligand production and copper speciation in an incubation experiment of Antarctic peninsula shelf waters from the Bransfield strait, southern ocean. *Marine Chemistry*, 122(1-4), pp.148-159.

- Behrenfeld, M. (2001). Biospheric primary production during an ENSO transition. *Science*, 291(5513), pp.2594-2597.
- Benning, L., Baker, A., Mihalopoulos, N., Carslaw, K., Bonneville, S., Jickells, T., Krom, M. and Shi, Z. (2012). Impacts on iron solubility in the mineral dust by processes in the source region and the atmosphere: A review. *Aeolian Research*, 5, pp.21-42.
- Bergquist, B., Wu, J. and Boyle, E. (2007). Variability in oceanic dissolved iron is dominated by the colloidal fraction. *Geochimica et Cosmochimica Acta*, 71(12), pp.2960-2974.
- Borghi, E., Morando, P. and Blesa, M. (1991). Dissolution of magnetite by mercaptocarboxylic acids. *Langmuir*, 7(8), pp.1652-1659.
- Bowie, A., Achterberg, E., Croot, P., de Baar, H., Laan, P., Moffett, J., Ussher, S. and Worsfold, P. (2006). A community-wide intercomparison exercise for the determination of dissolved iron in seawater. *Marine Chemistry*, 98(1), pp.81-99.
- Bowie, A., Achterberg, E., Mantoura, R. and Worsfold, P. (1998). Determination of sub-nanomolar levels of iron in seawater using flow injection with chemiluminescence detection. *Analytica Chimica Acta*, 361(3), pp.189-200.
- Bowie, A., Sedwick, P. and Worsfold, P. (2004). Analytical intercomparison between flow injection-chemiluminescence and flow injection-spectrophotometry for the determination of picomolar concentrations of iron in seawater. *Limnology and Oceanography: Methods*, 2(2), pp.42-54.
- Boyd, P., Butler, E., Nichols, C., Schoemann, V. and Hassler, C. (2010). Saccharides enhance iron bioavailability to southern ocean phytoplankton. *Proceedings of the National Academy of Sciences*, 108(3), pp.1076-1081.

- Bruland, K. and Rue, E. (1995). Complexation of iron(III) by natural organic ligands in the central north pacific as determined by a new competitive ligand equilibration/adsorptive cathodic stripping voltammetric method. *Marine Chemistry*, 50(1-4), pp.117-138.
- Buck, C., Landing, W. and Resing, J. (2013). Pacific Ocean aerosols: Deposition and solubility of iron, aluminum, and other trace elements. *Marine Chemistry*, 157, pp.117-130.
- Buck, C., Landing, W., Resing, J. and Lebon, G. (2006). Aerosol iron and aluminum solubility in the northwest Pacific Ocean: Results from the 2002 IOC cruise. *Geochemistry, Geophysics, Geosystems*, 7(4).
- Chen, M., Dei, R., Wang, W., and Guo, L. (2003). Marine diatom uptake of iron bound with natural colloids of different origins. *Marine Chemistry*, 81(3-4), pp.177-189.
- Chen, Y. (2004). Seasonal and spatial distributions and dry deposition fluxes of atmospheric total and labile iron over the tropical and subtropical North Atlantic Ocean. *Journal of Geophysical Research*, 109(D9).
- Chen, Y. and Siefert, R. (2003). Determination of various types of labile atmospheric iron over remote oceans. *Journal of Geophysical Research: Atmospheres*, 108(D24).
- Chen, Y., Meskhidze, N., Chuang, P. and Solomon, F. (2009). Acidic processing of mineral dust iron by anthropogenic compounds over the north pacific ocean. *Journal of Geophysical Research*, 114(D2).
- Colin, J., Caquineau, S., Desboeufs, K. and Journet, E. (2008). Mineralogy as a critical factor of dust iron solubility. *Geophysical Research Letters*, 35(7).
- Cornell, R., Posner, A. and Quirk, J. (1976). Kinetics and mechanisms of the acid dissolution of goethite (α -FeOOH). *Journal of Inorganic and Nuclear Chemistry*, 38(3), pp.563-567.

- Cornell, R., Rochelle M. and Schwertmann, U. (2003). *The iron oxides: Structure, properties, reactions, occurrences and uses*. 2nd ed. New York: Wiley-VCH Verlag GmbH.
- Croft, B., Pierce, J. and Martin, R. (2014). Interpreting aerosol lifetimes using the GEOS-Chem model and constraints from radionuclide measurements. *Atmospheric Chemistry and Physics*, 14(8), pp.4313-4325.
- Croot, P. and Baker, A. (2010). Atmospheric and marine controls on aerosol iron solubility in seawater. *Marine Chemistry*, 120(1-4), pp.4-13.
- Cullen, J. (1991). Hypotheses to explain high-nutrient conditions in the open sea. *Limnology and Oceanography*, 36(8), pp.1578-1599.
- de Baar, H. (2005). Synthesis of iron fertilization experiments: From the iron age in the age of enlightenment. *Journal of Geophysical Research*, 110(C9).
- de Baar, H., Sarthou, G., Timmermans, K., Veldhuis, M. and Gerringa, L. (2006). Covariance of dissolved Fe-binding ligands with phytoplankton characteristics in the Canary basin. *Marine Chemistry*, 102(3-4), pp.276-290.
- Doney, S. and Boyd, P. (2003). in *Ocean Biogeochemistry: A Synthesis of the Joint Global Ocean Flux Study*. M. J. R. Fasham, Ed, pp.157-193.
- Duckworth, O. and Martin, S. (2001). Surface complexation and dissolution of hematite by C1-C6 dicarboxylic acids at pH = 5.0. *Geochimica et Cosmochimica Acta*, 65(23), pp.4289-4301.
- Eggleston, C. and Samson, S. (1998). Active sites and the non-steady-state dissolution of Hematite. *Environmental Science & Technology*, 32(19), pp.2871-2875.

- Emmenegger, L., King, D., Sigg, L. and Sulzberger, B. (1998). Oxidation Kinetics of Fe(II) in a Eutrophic Swiss Lake. *Environmental Science & Technology*, 32(19), pp.2990-2996.
- Faivre, D. (2016). *Iron oxides: From Nature to Applications*. 1st ed. John Wiley & Sons, pp.32-33.
- Falkowski, P., Aiken, J., Kolber, Z., Bale, A. and Behrenfeld, M. (1996). Confirmation of iron limitation of phytoplankton photosynthesis in the equatorial pacific ocean. *Nature*, 383(6600), pp.508-511.
- Field, C. (1998). Primary production of the Biosphere: Integrating terrestrial and Oceanic components. *Science*, 281(5374), pp.237-240.
- Fitzsimmons, J., Bundy, R., Al-Subia, S., Barbeau, K. and Boyle, E. (2015). The composition of dissolved iron in the dusty surface ocean: An exploration using size-fractionated iron-binding ligands. *Marine Chemistry*, 173, pp.125-135.
- Fitzwater, S. and Martin, J. (1988). Iron deficiency limits phytoplankton growth in the north-east pacific subarctic. *Nature*, 331(6154), pp.341-343.
- Fu, H., Cwiertny, D., Carmichael, G., Scherer, M. and Grassian, V. (2010). Photoreductive dissolution of Fe-containing mineral dust particles in acidic media. *Journal of Geophysical Research*, 115(D11).
- Gao, Y., Xu, G., Zhan, J., Zhang, J., Li, W., Lin, Q., Chen, L. and Lin, H. (2013). Spatial and particle size distributions of atmospheric dissolvable iron in aerosols and its input to the Southern Ocean and coastal East Antarctica. *Journal of Geophysical Research: Atmospheres*, 118(22), pp.12,634-12,648.
- Gledhill, M. (2012). The organic complexation of iron in the marine environment: A review. *Frontiers in Microbiology*, 3.

- Gledhill, M. (2004). Production of siderophore type chelates by mixed bacterioplankton populations in nutrient enriched seawater incubations. *Marine Chemistry*, 88(1-2), pp.75-83.
- Grassian, V., Scherer, M., Carmichael, G., Cwiertny, D. and Fu, H. (2010). Photoreductive dissolution of Fe-containing mineral dust particles in acidic media. *Journal of Geophysical Research*, 115(D11).
- Hassler, C., Alasonati, E., Mancuso Nichols. and Slaveykova, V. (2011). Exopolysaccharides produced by bacteria isolated from the pelagic southern ocean — role in Fe binding, chemical reactivity, and bioavailability. *Marine Chemistry*, 123(1-4), pp.88-98.
- Hoffmann, M. and Johansen, A. (2003). Chemical characterization of ambient aerosol collected during the northeast monsoon season over the Arabian sea: Labile-Fe(II) and other trace metals. *Journal of Geophysical Research*, 108(D14).
- Hoffmann, M., Siefert, R. and Johansen, A. (2000). Chemical composition of aerosols collected over the tropical north Atlantic ocean. *Journal of Geophysical Research: Atmospheres*, 105(D12), pp.15277-15312.
- Hsu, S., Liu, S., Arimoto, R., Liu, T., Huang, Y., Tsai, F., Lin, F. and Kao, S. (2009). Dust deposition to the East China Sea and its biogeochemical implications. *Journal of Geophysical Research*, 114(D15).
- Hunter, K., In: Turner, D. and Watson, A. (2001). The biogeochemistry of iron in seawater. *John Wiley & Sons, London*, 6, pp.9-40.
- Hunter, K., Mackie, D. and Boyd, P. (2010). Aerosol iron deposition to the surface ocean — modes of iron supply and biological responses. *Marine Chemistry*, 120(1-4), pp.128-143.

- Jackson, G., Hunter, K., Sander, S., Ibisani, E. and Boyd, P. (2010). Remineralization of upper ocean particles: Implications for iron biogeochemistry. *Limnology and Oceanography*, 55(3), pp.1271-1288.
- Jickells, T. (2005). Global iron connections between desert dust, ocean Biogeochemistry, and climate. *Science*, 308(5718), pp.67-71.
- Jickells, T. and Baker, A. (2006). Mineral particle size as a control on aerosol iron solubility. *Geophysical Research Letters*, 33(17).
- Johansen, A. and Hoffmann, M. (2003). Chemical characterization of ambient aerosol collected during the northeast monsoon season over the Arabian Sea: Labile-Fe(II) and other trace metals. *Journal of Geophysical Research*, 108(D14).
- Johansen, A., Siefert, R. and Hoffmann, M. (2000). Chemical composition of aerosols collected over the tropical North Atlantic Ocean. *Journal of Geophysical Research: Atmospheres*, 105(D12), pp.15277-15312.
- Johnson, M. and Meskhidze, N. (2013). Atmospheric dissolved iron deposition to the global oceans: effects of oxalate-promoted Fe dissolution, photochemical redox cycling, and dust mineralogy. *Geoscientific Model Development*, 6(4), pp.1137-1155.
- Key, J. and Johansen, A. (2006). Photoreductive dissolution of ferrihydrite by methanesulfinic acid: Evidence of a direct link between dimethylsulfide and iron-bioavailability. *Geophysical Research Letters*, 33(14).
- King, D., Cooper, W., Rusak, S., Peake, B., Kiddle, J., O'Sullivan, D., Melamed, M., Morgan, C. and Theberge, S. (2007). Flow Injection Analysis of H₂O₂ in Natural Waters Using Acridinium Ester Chemiluminescence: Method Development and Optimization Using a Kinetic Model. *Analytical Chemistry*, 79(11), pp.4169-4176.

- Kohfeld, K., Harrison, S., Werner, M. and Tegen, I. (2004). Relative importance of climate and land use in determining present and future global soil dust emission. *Geophysical Research Letters*, 31(5).
- Kretzschmar, R., Halliday, A., Borer, P., Teutsch, N., Kraemer, S. and Wiederhold, J. (2006). Iron Isotope fractionation during proton-promoted, ligand-controlled, and Reductive dissolution of Goethite. *Environmental Science & Technology*, 40(12), pp.3787-3793.
- Kudela, R., Trasvina, A., Rollwagen, G., Constantinou, J., Landry, M., Cochlan, W., Cooper, D., Nightingale, P., Steinberg, P., Millero, F., Rogers, P., Sakamoto, C., Ferioli, L., Chavez, F., Tanner, S., Gordon, R., Fitzwater, S., Johnson, K. and Coale, K. (1996). A massive phytoplankton bloom induced by an ecosystem-scale iron fertilization experiment in the equatorial pacific ocean. *Nature*, 383(6600), pp.495-501.
- La Roche, J. and Geider, R. (1994). The role of iron in phytoplankton photosynthesis, and the potential for iron-limitation of primary productivity in the sea. *Photosynthesis Research*, 39(3), pp.275-301.
- Lee, Y., Pierce, J. and Adams, P. (2013). Representation of nucleation mode microphysics in a global aerosol model with sectional microphysics. *Geoscientific Model Development*, 6(4), pp.1221-1232.
- Lin, S., Dubovik, O., Holben, B., Prospero, J., Tegen, I., Chin, M. and Ginoux, P. (2001). Sources and distributions of dust aerosols simulated with the GOCART model. *Journal of Geophysical Research: Atmospheres*, 106(D17), pp.20255-20273.
- Liu, X. and Millero, F. (2002). The solubility of iron in seawater. *Marine Chemistry*, 77(1), pp.43-54.

- Lohan, M., Aguilar-Islas, A. and Bruland, K. (2006). Direct determination of iron in acidified (pH 1.7) seawater samples by flow injection analysis with catalytic spectrophotometric detection: Application and intercomparison. *Limnology and Oceanography: Methods*, 4(6), pp.164-171.
- Luther III, G., Butler, A., Witter, A. and Hutchins, D. (1999). Competition among marine phytoplankton for different chelated iron species. *Nature*, (400), pp.858-861.
- Mahowald, N. (2003). Mineral aerosol and cloud interactions. *Geophysical Research Letters*, 30(9).
- Maldonado, M., Barbeau, K., Robert, M., Cullen, J., Johnson, W., Bundy, R., Taylor, R. and Semeniuk, D. (2015). Iron-copper interactions in iron-limited phytoplankton in the northeast subarctic Pacific ocean. *Limnology and Oceanography*, 61(1), pp.279-297.
- Matsunaga, K., Nishioka, J. and Kuma, K. (1996). Controls on iron(III) hydroxide solubility in seawater: The influence of pH and natural organic chelators. *Limnology and Oceanography*, 41(3), pp.396-407.
- Mawji, E., Gledhill, M., Milton, J.A., Tarran, G.A., Ussher, S., Thompson, A., Wolff, G., Worsfold, P. and Achterberg, E. (2008). Hydroxamate siderophores: Occurrence and importance in the Atlantic ocean. *Environmental Science & Technology*, 42(23), pp.8675-8680.
- Mehra, O. (1958). Iron Oxide Removal from Soils and Clays by a Dithionite-Citrate System Buffered with Sodium Bicarbonate. *Clays and Clay Minerals*, 7(1), pp.317-327.
- Meskhidze, N. and Johnson, M. (2013). Atmospheric dissolved iron deposition to the global oceans: Effects of oxalate-promoted Fe dissolution, photochemical redox

- cycling, and dust mineralogy. *Geoscientific Model Development Discussions*, 6(1), pp.1901-1947.
- Miller, W., King, D., Lin, J. and Kester, D. (1995). Photochemical redox cycling of iron in coastal seawater. *Marine Chemistry*, 50(1-4), pp.63-77.
- Moffett, J. and Zika, R. (1987). Reaction kinetics of hydrogen peroxide with copper and iron in seawater. *Environmental Science & Technology*, 21(8), pp.804-810.
- Morel, F. (2003). The Biogeochemical cycles of trace metals in the oceans. *Science*, 300(5621), pp.944-947.
- Morel, F., Kustka, A. and Shaked, Y. (2005). A general kinetic model for iron acquisition by eukaryotic phytoplankton. *Limnology and Oceanography*, 50(3), pp.872-882.
- Paris, R., Desboeufs, K. and Journet, E. (2011). Variability of dust iron solubility in atmospheric waters: Investigation of the role of oxalate organic complexation. *Atmospheric Environment*, 45(36), pp.6510-6517.
- Plietker, B., Knolker, H. and Bauer, I. (2008). *Iron catalysis in organic chemistry: Reactions and applications*. Germany: Wiley-VCH Verlag GmbH.
- Powell, C., Baker, A., Church, T., Sedwick, P. and Sholkovitz, E. (2012). Fractional solubility of aerosol iron: Synthesis of a global-scale data set. *Geochimica et Cosmochimica Acta*, 89, pp.173-189.
- Prospero, J., Millero, F. and Trapp, J. (2010). Trends in the solubility of iron in dust-dominated aerosols in the equatorial Atlantic trade winds: Importance of iron speciation and sources. *Geochemistry, Geophysics, Geosystems*, 11(3).
- Pullin, M. and Cabaniss, S. (2001). Colorimetric flow-injection analysis of dissolved iron in high DOC waters. *Water Research*, 35(2), pp.363-372.

- Ramankutty, N., Feddema, J., Ballantine, J. and Mahowald, N. (2007). Global trends in visibility: Implications for dust sources. *Atmospheric Chemistry and Physics*, 7(12), pp.3309-3339.
- Resing, J., Landing, W. and Buck, C. (2010). Particle size and aerosol iron solubility: A high-resolution analysis of Atlantic aerosols. *Marine Chemistry*, 120(1-4), pp.14-24.
- Rich, H. and Morel, F. (1989). Bioavailability of well-defined iron(III) oxo hydroxo colloids to the marine diatom *Thalassiosira weissflogii*. *Journal of Inorganic Biochemistry*, 36(3-4), p.350.
- Roden, E., Kappler, A. and Konhauser, K. (2011). IRON IN MICROBIAL METABOLISMS. *Elements*, 7(2), pp.89-93.
- Rose, A. and Waite, T. (2001). Chemiluminescence of Luminol in the Presence of Iron(II) and Oxygen: Oxidation Mechanism and Implications for Its Analytical Use. *Analytical Chemistry*, 73(24), pp.5909-5920.
- Rue, E. and Bruland, K. (1997). The role of organic complexation on ambient iron chemistry in the equatorial Pacific Ocean and the response of a mesoscale iron addition experiment. *Limnology and Oceanography*, 42(5), pp.901-910.
- Salfity, J. and Regazzoni, A. (2000). *Interfacial chemistry of dissolving metal oxide particles: dissolution by organic acids. Chap. 14 Interfacial dynamics*. 1st ed. New York: M. Dekker, pp.513-540.
- Savoie, D., Prospero, J., Arimoto, R. and Duce, R. (1994). Non-sea-salt sulfate and methanesulfonate at American Samoa. *Journal of Geophysical Research*, 99(D2), p.3587.
- Schwertmann, U. (1991). Solubility and dissolution of iron oxides. *Plant and Soil*, 130(1-2), pp.1-25.

- Sedwick, P., Sholkovitz, E. and Church, T. (2007). Impact of anthropogenic combustion emissions on the fractional solubility of aerosol iron: Evidence from the Sargasso Sea. *Geochemistry, Geophysics, Geosystems*, 8(10).
- Shank, L. and Johansen, A. (2008). Atmospheric trace metal and labile iron deposition fluxes to the equatorial Pacific during EUCfe2006. *Ocean Sci. Meet.*
- Smoydzin, L. and von Glasow, R. (2007). Do organic surface films on sea salt aerosols influence atmospheric chemistry? - a model study. *Atmospheric Chemistry and Physics*, 7(21), pp.5555-5567.
- Srikanta Dani, K., Silva Benavides, A., Michelozzi, M., Peluso, G., Torzillo, G. and Loreto, F. (2017). Relationship between isoprene emission and photosynthesis in diatoms, and its implications for global marine isoprene estimates. *Marine Chemistry*, 189, pp.17-24.
- Stumm, W. and Furrer, G. (1987). The dissolution of oxides and aluminum silicates; examples of surface-coordination-controlled kinetics. *IN Aquatic surface chemistry*. 1st ed. New York: J. Wiley & Sons, pp.197-219.
- Sunda, W. (2001). Bioavailability and bioaccumulation of iron in the sea. *IUPAC Series on Analytical and Physical Chemistry of Environmental Systems*, 7, pp.41-84.
- Tindale, N., Liss, P., Hatton, A., Nightingale, P., Turner, S., Yungel, J., Swift, R., Hoge, F., Chisholm, S., Falkowski, P., Greene, R., Kolber, Z., Buck, K., Chavez, F., Sakamoto, C., Friederich, G., Zhang, J., Yao, W., Lee, K., Millero, F., Latasa, M., Ondrusek, M., Bidigare, R., Anderson, A., Collins, C., Stockel, J., Stanton, T., Ling, R., Liddicoat, M., Law, C., Van Scoy, K., Watson, A., Lindley, S., Barber, R., Coley, T., Nowicki, J., Elrod, V., Hunter, C., Tanner, S., Gordon, R., Fitzwater, S., Johnson, K., Coale, K. and Martin, J. (1994). Testing the iron hypothesis in ecosystems of the equatorial Pacific ocean. *Nature*, 371(6493), pp.123-129.

- Torrent, J. and Barrón, V. (1996). Surface Hydroxyl configuration of various crystal faces of Hematite and Goethite. *Journal of Colloid and Interface Science*, 177(2), pp.407-410.
- Trojanowicz, M. and Kołacińska, K. (2016). Recent advances in flow injection analysis. *The Analyst*, 141(7), pp.2085-2139.
- van der Merwe, P., Abemoschi, M., Grotti, M. and Lannuzel, D. (2015). Organic ligands control the concentrations of dissolved iron in Antarctic sea ice. *Marine Chemistry*, 174, pp.120-130.
- Wang, W. and Dei, R. (2003). Bioavailability of iron complexed with organic colloids to the cyanobacteria *Synechococcus* and *Trichodesmium*. *Aquatic Microbial Ecology*, 33, pp.247-259.
- Watanabe, S., Yamamoto, H. and Tsunogai, S. (1995). Dimethyl sulfide widely varying in surface water of the eastern North Pacific. *Marine Chemistry*, 51(3), pp.253-259.
- Watson, A., Turner, S., Tsuda, A., Takeda, S., Smetacek, V., Schoemann, V., Sarmiento, J., Rivkin, R., Pollard, R., Owens, N., Levasseur, M., Lancelot, C., Harvey, M., Follows, M., de Baar, H., Cullen, J., Coale, K., Buesseler, K., Boyle, E., Blain, S., Law, C., Jickells, T. and Boyd, P. (2007). Mesoscale iron enrichment experiments 1993-2005: Synthesis and future directions. *Science*, 315(5812), pp.612-617.
- White, E., Vaughan, P. and Zepp, R. (2003). Role of the photo-Fenton reaction in the production of hydroxyl radicals and photobleaching of colored dissolved organic matter in a coastal river of the southeastern United States. *Aquatic Sciences - Research Across Boundaries*, 65(4), pp.402-414.
- Wu, J. (2001). Soluble and Colloidal Iron in the Oligotrophic North Atlantic and North Pacific. *Science*, 293(5531), pp.847-849.

- Xiao, D., Guo, Y., Lou, X., Fang, C., Wang, Z. and Liu, J. (2014). Distinct effects of oxalate versus malonate on the iron redox chemistry: Implications for the photo-Fenton reaction. *Chemosphere*, 103, pp.354-358.
- Yokouchi, Y., Li, H., Machida, T., Aoki, S. and Akimoto, H. (1999). Isoprene in the marine boundary layer (southeast Asian Sea, eastern Indian Ocean, and Southern Ocean): Comparison with dimethyl sulfide and bromoform. *Journal of Geophysical Research: Atmospheres*, 104(D7), pp.8067-8076.
- Yuan, J. and Shiller, A. (2005). Distribution of hydrogen peroxide in the northwest Pacific Ocean. *Geochemistry, Geophysics, Geosystems*, 6(9).
- Zepp, R., Faust, B. and Hoigne, J. (1992). Hydroxyl radical formation in aqueous reactions (pH 3-8) of iron(II) with hydrogen peroxide: the photo-Fenton reaction. *Environmental Science & Technology*, 26(2), pp.313-319.
- Zhang, Y., Kallay, N. and Matijevic, E. (1985). Interaction of metal hydrous oxides with chelating agents. 7. Hematite-oxalic acid and -citric acid systems. *Langmuir*, 1(2), pp.201-206.
- Zhu, X., Prospero, J. and Millero, F. (1997). Diel variability of soluble Fe(II) and soluble total Fe in North African dust in the trade winds at Barbados. *Journal of Geophysical Research: Atmospheres*, 102(D17), pp.21297-21305.
- Zubkov, M., Williamson, R., Venables, H., Thomalla, S., Taylor, S., Stinchcombe, M., Smith, T., Seeyave, S., Read, J., Poulton, A., Popova, E., Planquette, H., Nielsdóttir, M., Nédélec, F., Morris, P., Lampitt, R., Jickells, T., Hughes, J., Holland, R., Hickman, A., French, M., Fones, G., Fielding, S., Charette, M., Bakker, D., Baker, A., Allen, J., Statham, P., Mills, R., Moore, C., Lucas, M., Sanders, R., Salter, I. and Pollard, R. (2009). Southern ocean deep-water carbon export enhanced by natural iron fertilization. *Nature*, 457(7229), pp.577-580.

APPENDIX

Table A1. Size resolved Fe(II) concentrations in the equatorial Pacific Ocean region: volume weighted averages, standard deviations (SD), medians, ranges, and sample numbers (N). P value for Student's t-test performed between pervious stage and current stage (P). Units are Fe (pg m^{-3}).

Initial (0-0.3 seconds)				
Particle Size Fraction	Ave	SD	Median	N
Large	0.81	1.03	0.69	32
Coarse	5.37	6.77	4.95	38
Fine	12.66	10.08	11.96	34
UF	14.04	16.37	14.02	33
Dark (0.3-20 seconds)				
Particle Size Fraction	Ave	SD	Median	P
Large	0.19	0.50	0.00	0.00
Coarse	5.34	6.46	4.64	0.99
Fine	13.43	11.23	12.64	0.73
UF	18.16	19.24	18.40	0.29
Light (20-75 seconds)				
Particle Size Fraction	Ave	SD	Median	P
Large	0.36	0.89	0.00	0.22
Coarse	14.63	12.46	11.64	0.00
Fine	23.94	24.39	22.07	0.02
UF	30.34	29.66	30.52	0.02
ED 1 st (75-180 seconds)				
Particle Size Fraction	Ave	SD	Median	P
Large	0.16	0.63	0.00	0.15
Coarse	17.78	17.16	13.28	0.33
Fine	34.67	37.09	25.46	0.16
UF	35.13	32.59	34.11	0.46
ED 2nd (180-285 seconds)				
Particle Size Fraction	Ave	SD	Median	P

Large	0.29	1.48	0.00	0.62
Coarse	19.14	18.31	15.13	0.72
Fine	38.80	37.87	28.83	0.65
UF	43.61	42.93	40.82	0.28

Table A2. Size resolved atmospheric iron concentrations in the equatorial Pacific Ocean region: volume weighted averages, standard deviations (SD), medians.

North Equatorial Pacific Ocean Region			
Particle Size Fraction	Ave	SD	Median
	Fe(II) (pg m-3)		
Large	0.000	0.000	0.000
Coarse	26.443	27.888	23.721
Fine	38.293	25.189	29.539
UF	28.849	25.189	32.557

Central Equatorial Pacific Ocean Region			
Particle Size Fraction	Ave	SD	Median
	Fe(II) (pg m-3)		
Large	0.501	1.910	0.000
Coarse	10.085	8.006	8.470
Fine	38.184	41.389	24.928
UF	56.437	43.334	40.822

West Equatorial Pacific Ocean Region			
Particle Size Fraction	Ave	SD	Median
	Fe(II) (pg m-3)		
Large	0.239	0.648	0.000
Coarse	26.411	24.173	23.255
Fine	38.491	34.533	26.669
UF	40.359	25.543	47.194

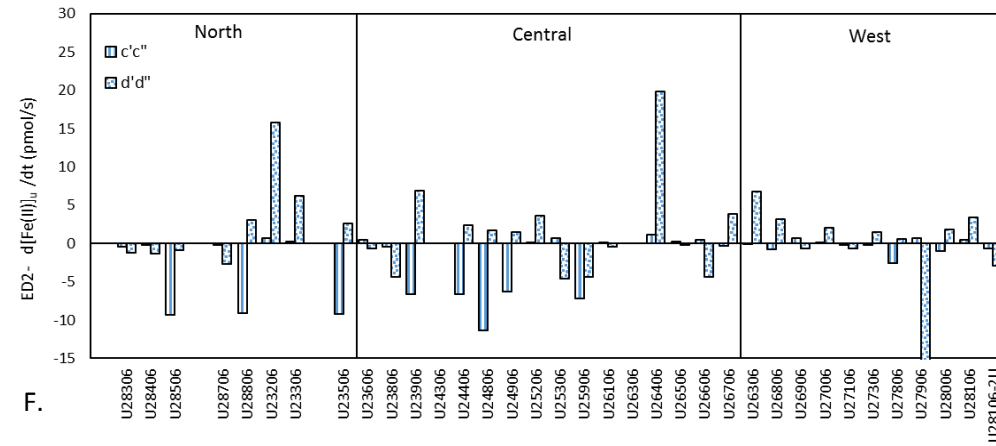
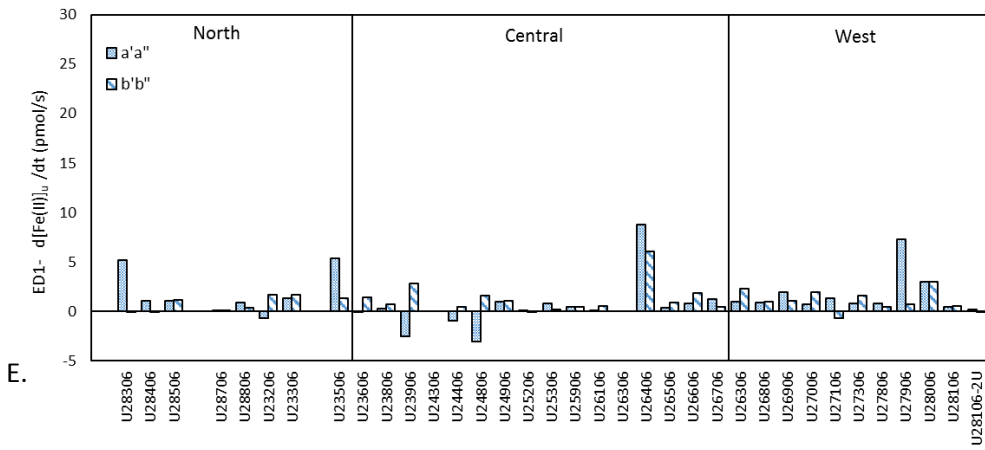
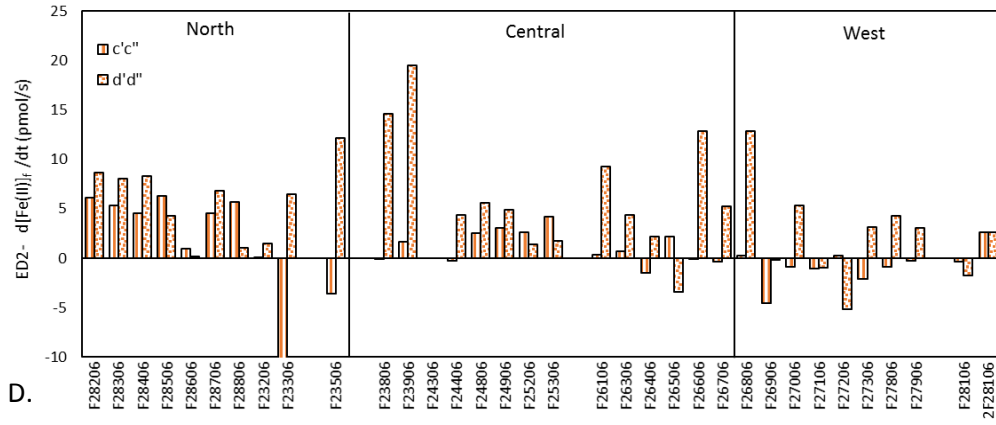
Table A3. Volume weighted average Fe(II) concentration in various size fractions, stages, and regions were compared using Student's t-test. Ratios of the respective number are shown in the table (A/B) (top) and those with p-values (bottom) smaller than 0.05 are marked red to indicate significant differences. Number in red indicate those that displayed a significant difference which were primarily seen from dark to light in the coarse, fine, and ultrafine size fractions by the ratio of 2.74, 1.78 and 1.67.

2A		B		Coarse		Fine		Ultrafine	
				Central	North	Central	North	Central	North
				Ratio of volume weighted average					
Initial	West	Ratio of volume weighted average	0.692	0.908	0.667	0.570	1.403	0.704	
	Central			1.311		0.856		0.502	
Light	West		0.588	0.812	0.840	0.746	1.295	0.618	
	Central			1.383		0.840		1.294	
ED2 nd	West		2.620	1.000	1.000	0.990	0.715	0.715	
	Central			2.632		1.010		0.511	

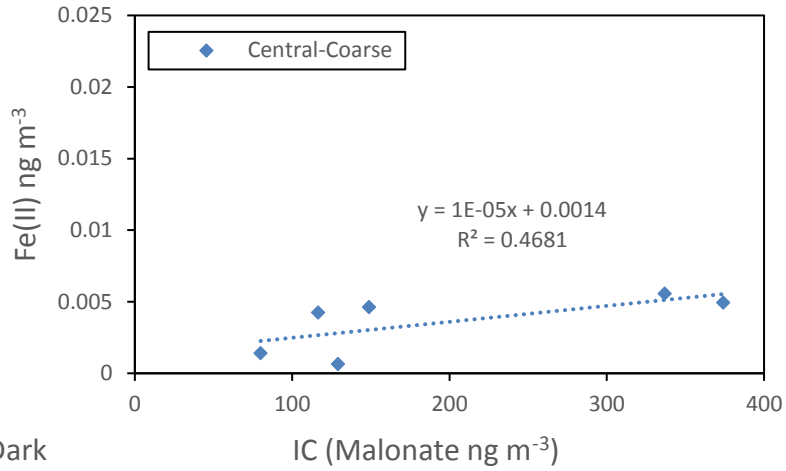
				Coarse		Fine		Ultrafine	
				Central	North	Central	North	Central	North
				P values					
Initial	West	P values	0.263	0.532	0.082	0.017	0.194	0.172	
	Central			0.446		0.527		0.023	
Light	West		0.029	0.489	0.499	0.166	0.266	0.110	
	Central			0.392		0.715		0.009	
ED2 nd	West		0.002	0.997	0.977	0.984	0.198	0.357	
	Central			0.080		0.993		0.040	

Table A4: Summary of Fe(II) correlation to anions. The same size fraction/stage are marked with the same color.

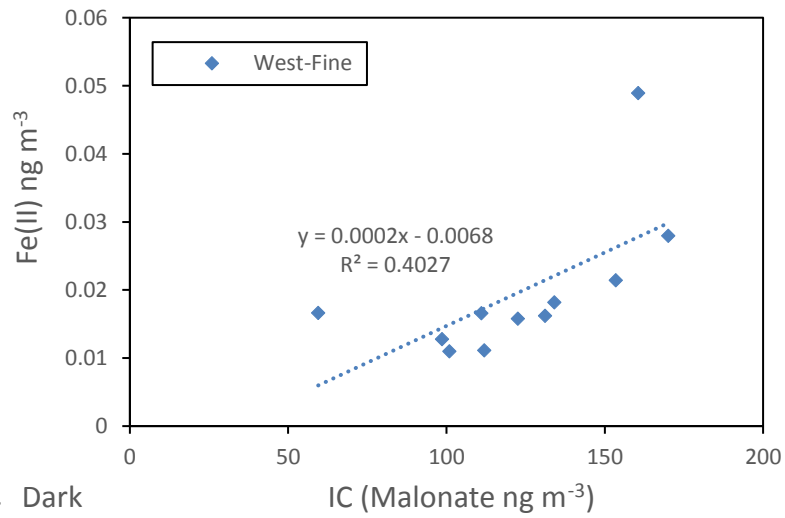
	North	Central	West
Malonate	Coarse, Dark Fe	Fine, Dark Fe Ultrafine, Light Fe	
Oxalate	Coarse, Light Fe	All fractions, Dark Fe	
nss-SO42-	Fine, Dark Fe; Fine, Light Fe		Fine, Light Fe
MSA	Coarse, Light Fe		Fine, Light Fe
Fe total			Coarse, Dark Fe; Ultrafine, Light Fe



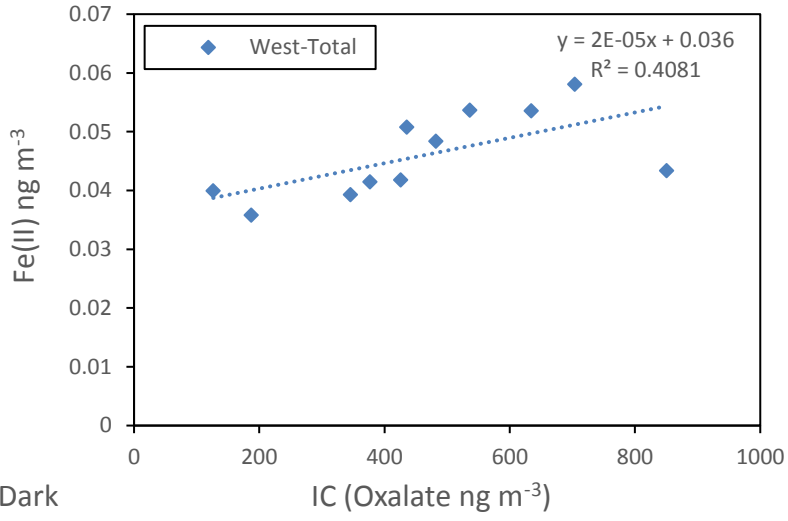
Figures A2 (A-L). Fe(II) concentrations vs. various anions and total Fe (in ng m^{-3}). Only results with correlation coefficient of $R^2 > 0.2$ are shown.



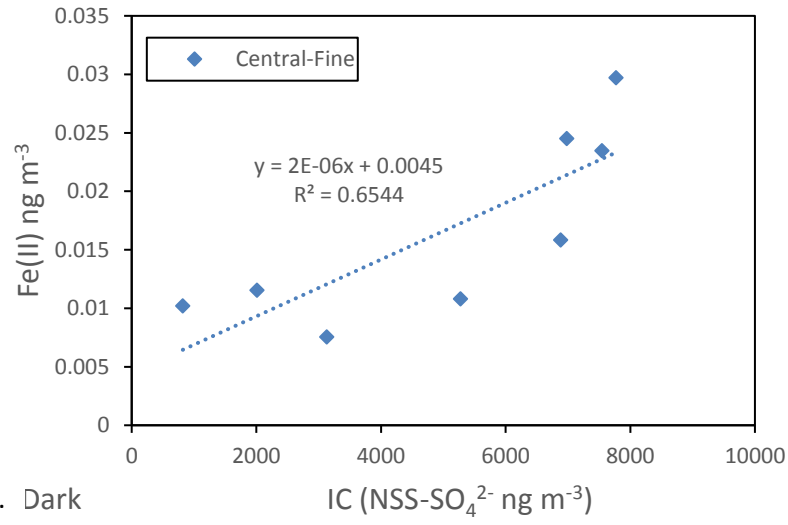
A. Dark



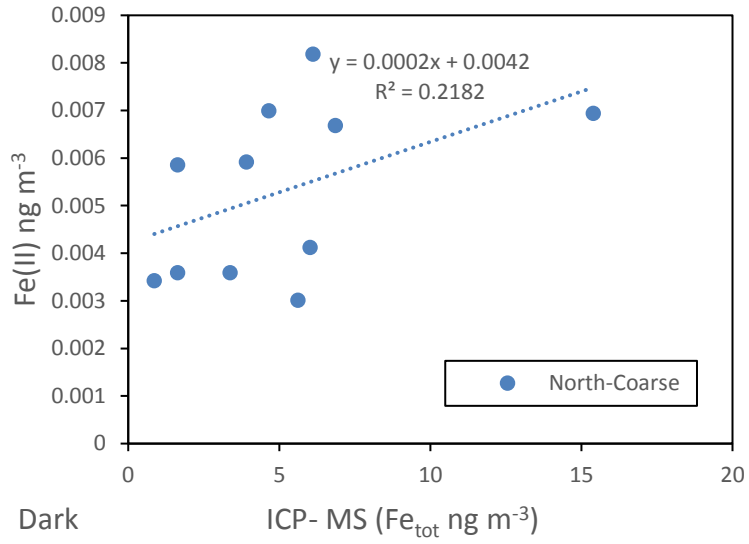
B. Dark



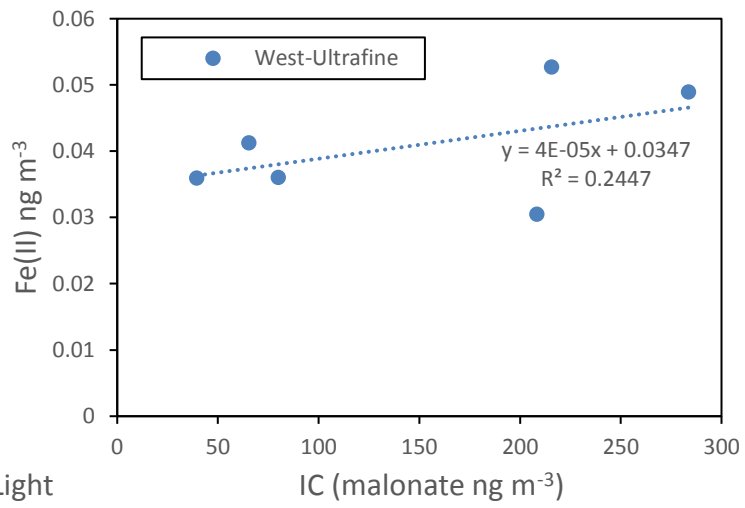
C. Dark



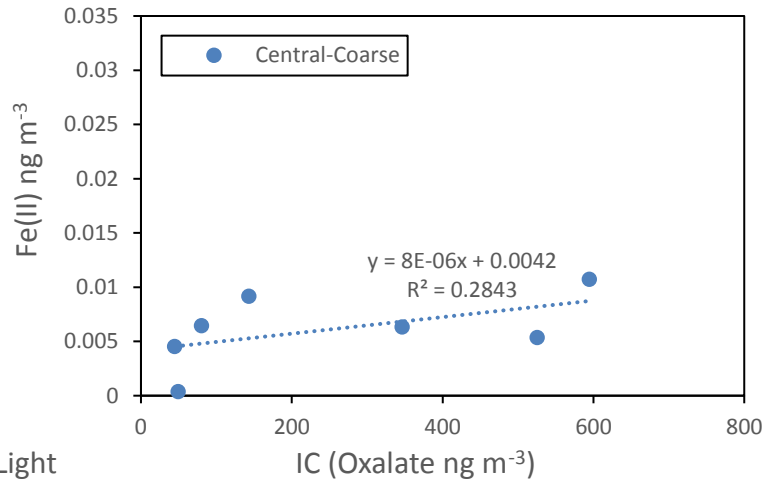
D. Dark



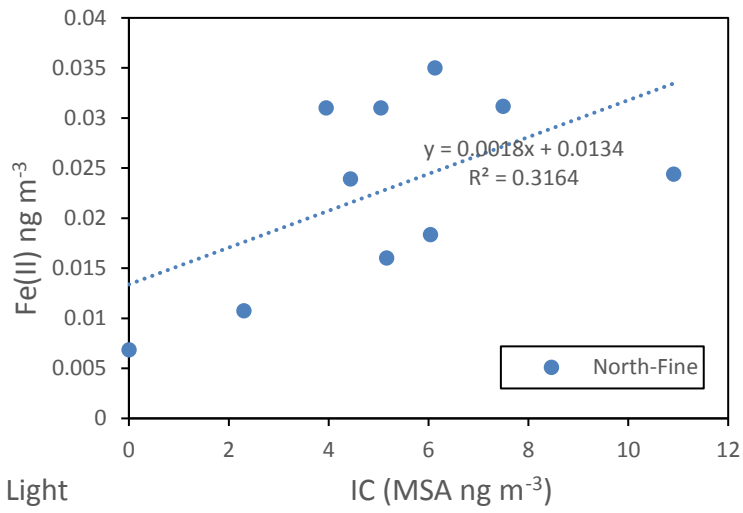
E. Dark



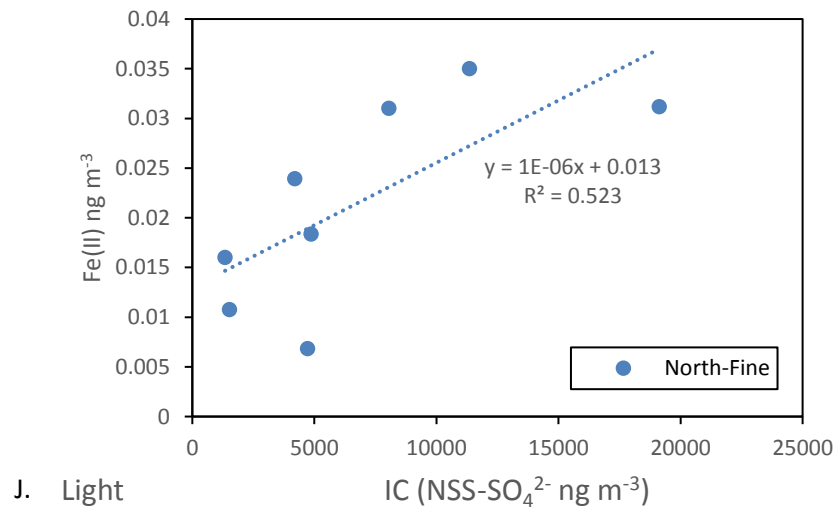
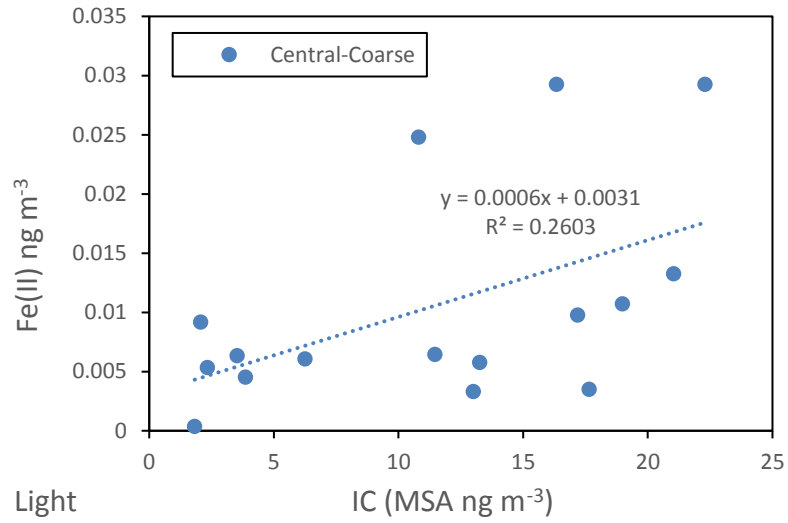
F. Light

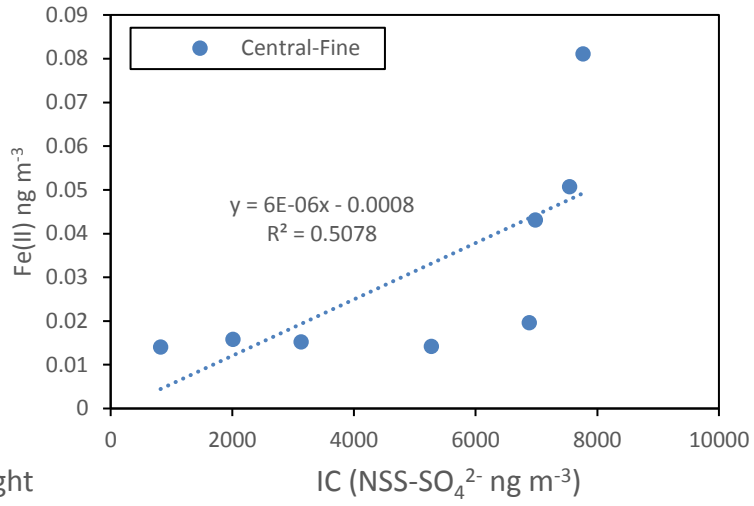


G. Light

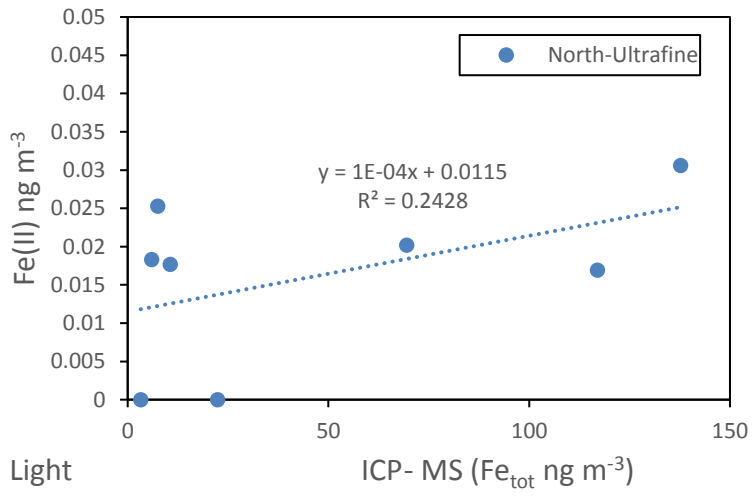


H. Light



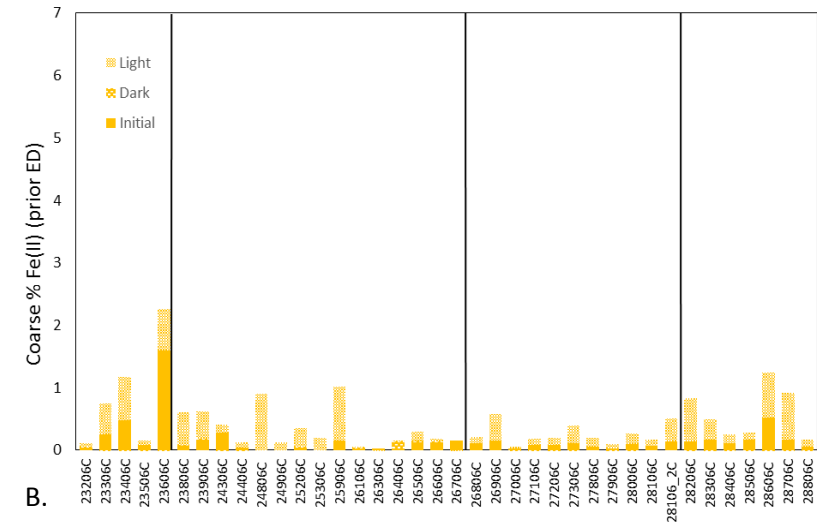
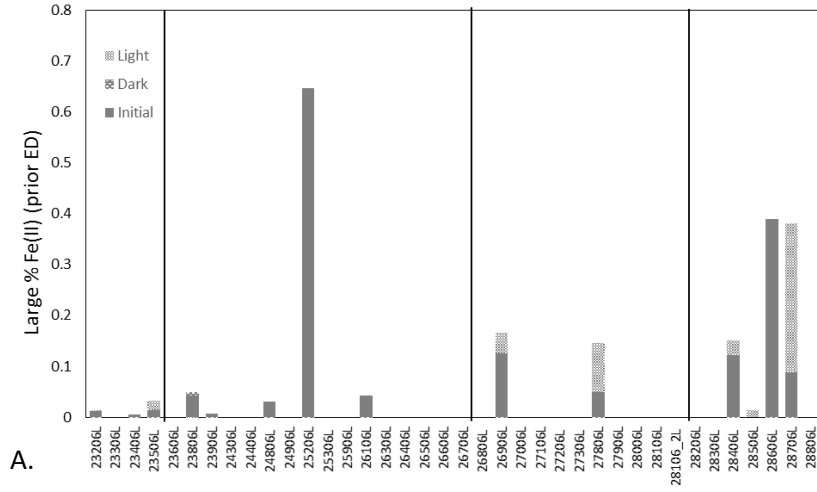


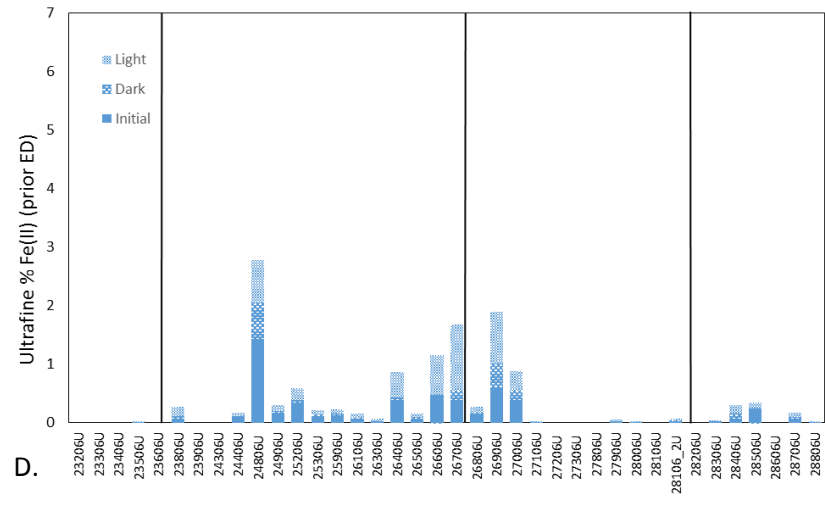
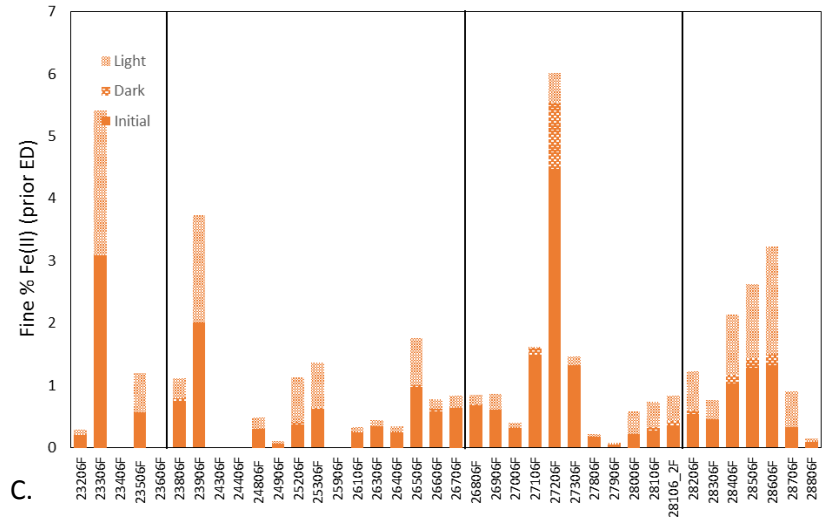
K. Light



L. Light

Figures A3 (A-D). Fe(II) contribution from first three stages in each sample. The percentage of Fe(II) contribution of total Fe from stage to stage before ED.





Figures 4 (A-D). The percentage of Fe(II) contribution of total Fe from stage to stage after ED.

